AIAA JOURNAL
Vol. 59, No. 11, November 2021

Aircraft to Ground Profiling: Turbulence Measurements and Optical System Performance Modeling

Yakov Diskin,* Matthew Whiteley,† Mitchell Grose,‡ Kevin Jackovitz,§ Richard Drye,¶ Brandon Hampshire,** Monte Owens,†† Eric Smith,‡‡ and Eric Magee§§
MZA Associates Corporation, Dayton, Ohio 45430
Matthew Kalensky,¶¶ Eric Jumper,*** and Stanislav Gordeyev†††
University of Notre Dame, Notre Dame, Indiana 46556
and
Aaron Archibald‡‡‡
Air Force Institute of Technology, Wright–Patterson Air Force Base, Ohio 45433

https://doi.org/10.2514/1.J060580

A series of flight experiments have demonstrated a novel approach to measuring path-resolved optical turbulence quantities, such as C_n^2, along an air-to-ground slant path. This paper describes the data acquisition experiments that involved two laser beams propagating between an orbiting airborne platform and a stationary ground terminal over an 8 km slant path. Ground-based and in-flight measurements were collected simultaneously, and C_n^2 profiles were computed using the difference of differential-tilt variance (DDTV) technique. This paper describes the DDTV technique that enables the path-resolved measurement of turbulence strength resulting in C_n^2 profiles. The resulting turbulence profiles reveal what is believed to be the aero-optical contamination from the aircraft boundary layer within the statistics closest to the aircraft. Therefore, the contamination of the aero-optical environment can be quantified with respect to the rest of the atmospheric propagation path. Lastly, this paper presents analyses that compare the measured atmospheric turbulence profiles to state-of-the-art atmospheric models. The analyses extend beyond C_n^2 comparisons and show the measurement-versus-modeling comparison in terms of key directed energy system propagation parameters such as Greenwood frequency, coherence diameter, Rytov number, isoplanatic angle, Tyler frequency, open-loop jitter, and open-loop Strehl ratio. The slant path turbulence is analyzed in the context of air-to-ground and ground-to-air directed energy systems.

Nomenclature

a	=	atmospheric tilt covariances
b	=	source separation
C_f	=	skin friction coefficient
C_n^2	=	refractive-index structure constant of turbulence, measures turbulence strength
D	=	aperture diameter
d	=	tilts
K_{GD}	=	Gladstone–Dale constant
L	=	propagation path length
M	=	Mach number
OPD_{RMS}	=	root mean square of optical path difference
r_0	=	spherical-wave coherence diameter
W	=	weighting normalization constants
w	=	weighting functions
z	=	location along the propagation path
α	=	scaling factor based on atmospheric coherence lengths
Γ	=	gamma function
Δx	=	subaperture separation
δ	=	boundary-layer thickness
θ_0	=	isoplanatic angle
κ	=	wavenumber
λ	=	wavelength
ξ	=	normalized path position
ρ_∞	=	freestream density
σ_χ	=	Rytov parameter
σ_δ	=	difference of differential-tilt variance parameter
σ_{HO}^2	=	tilt-removed phase variance

Presented as Paper 2020-0682 at the AIAA Scitech 2020 Forum, Orlando, FL, January 6–10, 2020; received 26 January 2021; revision received 27 March 2021; accepted for publication 1 April 2021; published online 3 June 2021.

*Vice President and Senior Scientist; matthew.whiteley@mza.com.
†Research Engineer; yakov.diskin@mza.com.
‡Scientist; Mitchell.Grose@mza.com.
§Research Engineer; Kevin.Jackovitz@mza.com.
¶Scientist; Richard.Drye@mza.com.
**Engineer; Brandon.Hampshire@mza.com.
††Senior Scientist; Monte.Owens@mza.com.
‡‡Scientist; Eric.Smith@mza.com.
§§Senior Scientist; Eric.Magee@mza.com.
¶¶Graduate Researcher, Aerospace and Mechanical Engineering Department; mkalensk@nd.edu. Student Member AIAA (Corresponding Author).
***Aero-Optics Group Director, Roth-Gibson Professor, Aerospace and Mechanical Engineering Department; ejumper@nd.edu. Fellow AIAA.
†††Associate Professor, Aerospace and Mechanical Engineering; Stanislav.V.Gordeyev.1@nd.edu. Associate Fellow AIAA.
‡‡‡Research Associate; Aaron.Archibald@afit.edu.

I. Introduction

RECENTLY, there has been interest in the use of laser and other optical systems mounted on a flight vehicle for a variety of applications, such as directed energy, optical communication, and reconnaissance systems [1–5]. The fluctuations in the refractive index, or optical turbulence, in the atmospheric medium affect the performance of these optical systems when a beam is propagated through the atmosphere. There are many system and engagement parameters that could influence an optical system's sensitivity to turbulence. Atmospheric turbulence conditions fluctuate continuously with changes in weather, terrain, and altitude. Thus, for long propagation geometries, especially slant path geometries, the turbulence at one end of the path is often drastically different from that at the other end. Atmospheric turbulence obstructs the spatial coherence of a laser beam as it is transmitted through the atmosphere, and for airborne directed energy system applications, it can drastically hinder the degree that the laser can be focused on a target [6]. However, if the aberrations imposed on the laser are measurable, adaptive optics technology can compensate

for the distortions and alleviate the undesirable effects. A thorough understanding of the turbulence encountered along a path is necessary for adaptive optics system designers [7].

In this work, turbulence profiling experiments are conducted that seek to measure turbulence strength along a path from a stationary ground station to an orbiting aircraft station. The flight experiments and corresponding analyses described in this paper have three major contributions to the atmospheric sciences and directed energy communities:

1) A novel method to take air-to-ground path-resolved turbulence profiling measurements is presented.

2) Unique decoupling processing techniques are employed that allow atmospheric and aero-optical induced effects to be analyzed separately.

3) The measurement results are compared against state-of-the-art atmospheric turbulence models. The measured and modeled turbulence profiles are analyzed with respect to how they impact directed energy system performance.

The paper is organized as follows. The path-resolved turbulence profiling algorithm used is described in Sec. II. The experimental setup and data collection process are described in Sec. III. The recorded turbulence measurements are affected by the aero-optical boundary layer of the aircraft, and the anticipated magnitude of the aero-optical contamination in the turbulence profiles is discussed in Sec. IV. In Sec. V, the measured turbulence profiles are compared with state-of-the-art atmospheric models. This section also describes the unique decoupling technique that enables the aero-optical contamination to be isolated and removed from the rest of the atmospheric turbulence analysis. In Sec. VI, the modeling-versus-measurement analysis examines how differences in turbulence profiles impact directed energy system performance parameters. The results are presented in the context of air-to-ground and ground-to-air directed energy systems propagating along the same slant path. The key findings are summarized and concluded in Sec. VII.

II. Difference of Differential Tilt Variances Profiling

The atmospheric refractive index structure parameter C_n^2 is a measure of optical turbulence strength [6,8]. Measuring C_n^2 at various positions along a path is typically referred to as turbulence profiling [9]. Many researchers have investigated the measurement of atmospheric optical turbulence characteristics using a variety of approaches [10–21]. The turbulence profiler used in this work, referred to as a path-resolved optical profiling system (PROPS), computes path-resolved measurements by using multiple point sources (red and blue) on the one end of the path and multiple observing subapertures in a Shack–Hartmann wavefront sensor (SHWFS) on the other. Ray paths from two subapertures can cross and reveal information about a particular part of the propagation path. The profiler uses a cooperative source and wavefront sensor to measure the C_n^2 profile by calculating subaperture tilt variations. The profiling technique computes the difference of differential-tilt variance (DDTV) to make path-resolved optical turbulence measurements.

Generally, measuring optical turbulence along a path is challenging, especially if the path altitude above ground level is not constant. Rytov theory is the primary basis for turbulence approximations resulting from optical wave propagation along a path [6,8,9]. The Rytov parameter σ_χ^2 can be related to parameters such as C_n^2 by use of Eq. (1):

$$\sigma_\chi^2 = 0.5631\left(\frac{2\pi}{\lambda}\right)^{7/6}\int_0^L C_n^2(z)\left[z\left(1-\frac{z}{L}\right)\right]^{5/6}\mathrm{d}z \tag{1}$$

where λ is the wavelength, z is the position along the path, and L is the full path length. Equation (1) is valid in propagation scenarios of weak turbulence ($\sigma_\chi^2 \leq 0.3$). In instances of strong turbulence or for long propagation path lengths, scintillation saturates and the Rytov parameter is no longer useful in generating meaningful turbulence approximations [22]. With the amendable nature of Rytov theory for calculating integrated optical turbulence strength parameters, we seek to extend the breadth of situations in which this theoretical construct can be applied. Rather than use irradiance-based quantities, the work described here uses the DDTV, first outlined and presented in Ref. [9], to produce meaningful statistics for computing turbulence parameters. The DDTV measurements are proportional to the Rytov parameter and can be used to estimate the value of the integral expression in Eq. (1) [9]. This method relies on phase data, avoiding the issue of saturation. The DDTV technique uses differential statistics and thus also avoids contamination from undesirable gimbal motion and additive noise [9,23].

The DDTV method uses an arbitrary number of sources and subapertures separated by a propagation range. The sources themselves are physically separated by a distance b considered small relative to the propagation path L. On the side receiving the light from the sources is a subaperture array where each subaperture is separated from the others by varying distances, Δx. The light from the sources is initially undisturbed. As the light propagates through the atmosphere, the small spatially and temporally dependent fluctuations in the atmosphere's refractive index perturb the light causing its departure from planarity. Using an SHWFS, each subaperture focuses the light it receives to a point creating an array of discrete illuminated spots, or centroids. The incoming light is filtered to observe the light received from each source. The x and y deviations, local tilts of the centroids away from their time resolved expected spatial locations, are an indication of the local deviation from planarity of the incoming light. The geometry of the source/aperture arrangement enables the existence of locations along the path where light emitted from the sources crosses paths with the light received through different subaperture pairs. At these locations, there is a commonality in how the light is affected by the surrounding physical environment. Figure 1 illustrates the source/aperture schematic. By analyzing different combinations of subaperture separations, the crossing of the beams is moved to different parts of the propagation path. For widely separated subapertures and fixed sources, the crossing point is far from the receiving aperture as seen in the top illustration in Fig. 1. For minimally separated (side by side) subapertures, the crossing point is very close to the SHWFS as shown in the bottom illustration in Fig. 1. In this diagram, a yellow circle highlights the location where the red (R) and blue (BL) light cross paths for a particular subaperture pair combination.

The DDTV approach is applied from acquired tilt data as

$$\sigma_\delta^2 = \langle (d_{R1} - d_{\mathrm{BL}2})^2\rangle - \langle (d_{R2} - d_{\mathrm{BL}1})^2\rangle \tag{2}$$

where σ_δ^2 is the DDTV measurement computed from d, which represents the local tilts for different subaperture/source combinations. Subscripts R and BL indicate the light source and red and blue, respectively. Subscripts "1" and "2" represent the subapertures receiving the light source. Each local tilt measurement is a combination of atmospheric tilt as well as noise and platform motion components. After expanding, simplifying, and ignoring the negligible components of Eq. (2) [9,23], only the difference in atmospheric tilt covariances, a, remains as

$$\sigma_\delta^2 = 2\Big(\langle a_{R1}a_{BL2}\rangle - \langle a_{R2}a_{BL1}\rangle\Big) \tag{3}$$

For two subapertures separated by a physical distance Δx, the covariance of Zernike x-tilt coefficients can be calculated using

$$\langle a_1 a_2\rangle = 16\sqrt{3}\Gamma(8/3)\left(\frac{2\pi}{\lambda}\right)^2 D^{5/3}L\int_0^L C_n^2(z)W(\xi)\mathrm{d}\xi \tag{4}$$

where D is the subaperture diameter, and ξ is the normalized position along the path defined by z/L [24–26]. Therefore, the covariance for a specific $C_n^2(z)$ is a function of the normalized aperture and source separation. The $W(\xi)$ term represents a weighting function applied to the expression. Equation (4) can easily be substituted into the result determined from the DDTV geometry and, with simplification, yields

$$\sigma_\delta^2 = \frac{128\sqrt{3}\Gamma(8/3)}{\pi^2}\left(\frac{2\pi}{\lambda}\right)^2 D^{5/3}L\int_0^L C_n^2(z)(W_{0c}w_c(\xi) - W_0 w(\xi))\mathrm{d}\xi \tag{5}$$

This result produces an expression for the DDTV parameter with C_n^2 embedded in this weighted integral equation. Here, W_{0c} and W_0 are

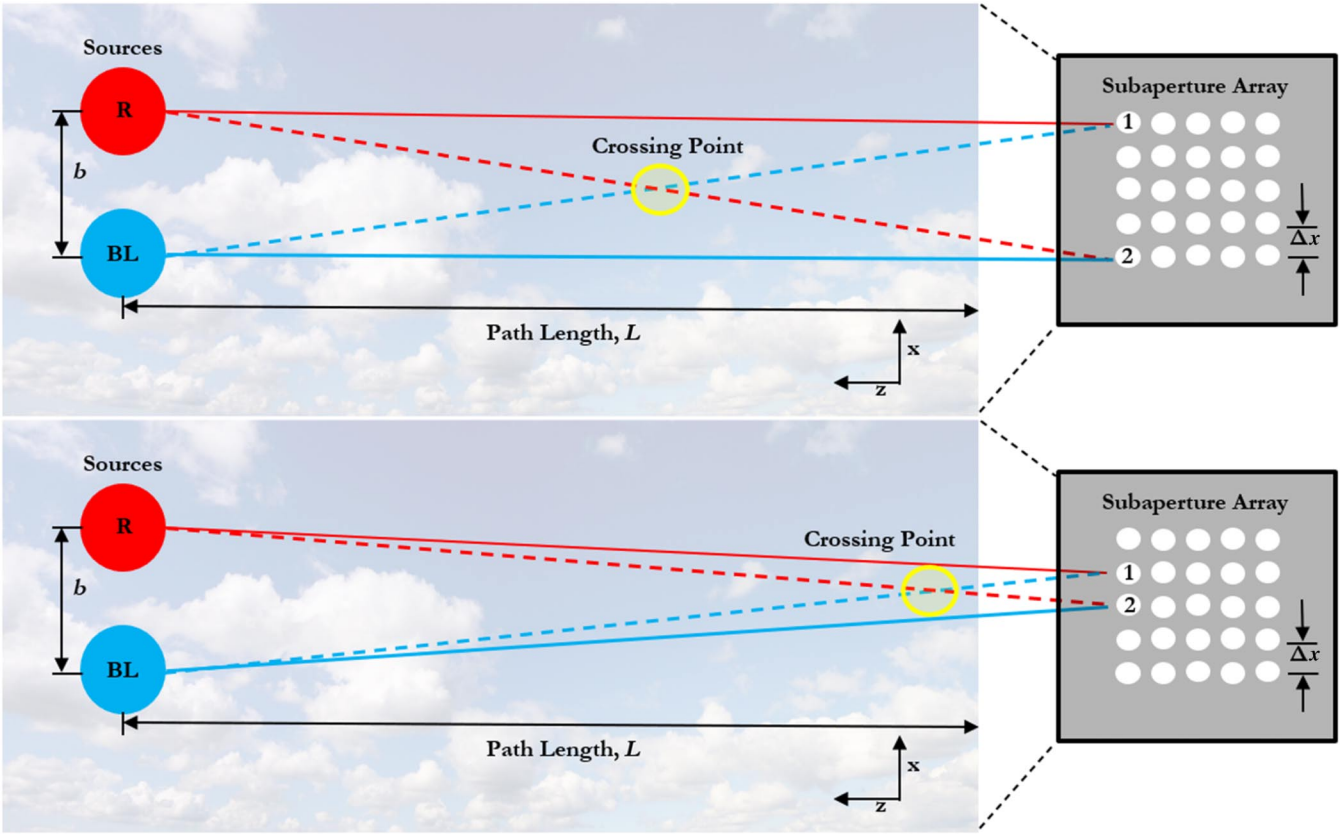

Fig. 1 Schematic of the DDTV hardware setup. Various combinations of subaperture separations enable path resolved turbulence profiling.

normalization constants, and $w_c(\xi)$ and $w(\xi)$ are weighting functions for the cross-path and non-cross-path geometries, respectively. If the known quantities in Eq. (5) are gathered into a quantity m as

$$m_j = \frac{\sigma_\delta^2}{128\sqrt{3}\Gamma(8/3)/\pi^2(2\pi/\lambda)^2 D^{5/3} LW} \tag{6}$$

then Eq. (5) can be rearranged to form a linear system,

$$\begin{bmatrix} m_1 \\ \vdots \\ m_J \end{bmatrix} = \begin{bmatrix} p_{11} & \cdots & p_{1K} \\ \vdots & \ddots & \vdots \\ p_{J1} & \cdots & p_{JK} \end{bmatrix} \begin{bmatrix} C_{n_1}^2 \\ \vdots \\ C_{n_K}^2 \end{bmatrix} \tag{7}$$

Here, p is a matrix of weighting functions for J number of DDTV measurements by K number of propagation path partitions. Using the pseudomatrix inverse, C_n^2 can be calculated for partitions along the path. A more thorough explanation of the procedure and theoretical construct behind DDTV can be found in Refs. [9,23].

The curves shown in the left plot of Fig. 2 illustrate how different weights are applied along the propagation path based on the DDTV geometry. The solid blue curve represents the scenario in Fig. 1, where source R is received by aperture 1 and source BL is received by aperture 2, referred to as the separate path geometry. The red dashed line in the left plot of Fig. 2 represents when source R is received by aperture 2 and source BL is received by aperture 1, otherwise referred to as the cross-path geometry. At the intersection of the red and blue light, the same turbulence environment is experienced. Therefore, the

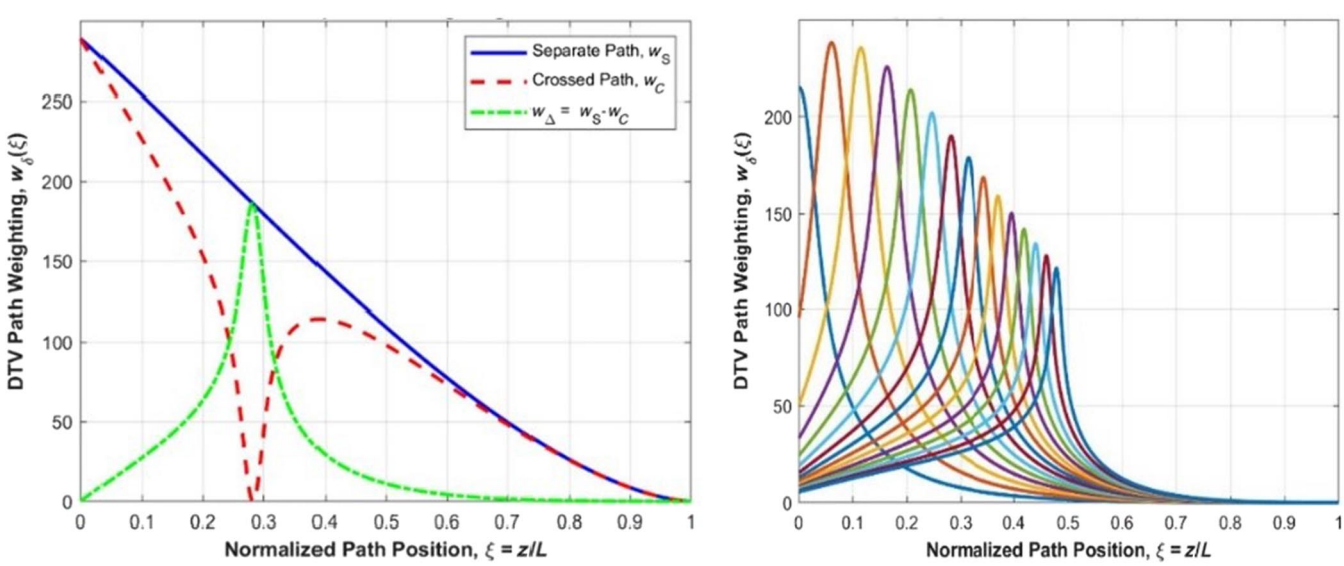

Fig. 2 Path weighting for separate path and cross path scenarios.

DDTV technique computes the difference between the separate path and the cross-path weighting functions to produce a new weighting function, shown by the green line in the left plot of Fig. 2, which has sensitivity to the specific portion of the path where the red and blue intersect. Different subaperture pairs change the location along the path where the sources intersect. Consequently, the point on the path where the weight is applied also changes. This method is applied to all source/subaperture combinations resulting in a set of DDTV weighting functions that resolve the path as seen in the right plot of Fig. 2. The plot shows the weighting functions covering approximately 50% of the full propagation path closest to the subaperture array. Therefore, to obtain full path sensitivity a second profiler system is setup in the opposite configuration to have sources and an SHWFS on both ends of the path.

III. Experimental Setup and Data Acquisition Campaign

A. Data Acquisition

The 2019 turbulence profiling flight campaign [27,28] in Grand Rapids, Michigan, aimed to collect air-to-ground path-resolved turbulence measurements for comparison and validation with state-of-the-art atmospheric turbulence models. This was the third campaign of its kind, with the first two occurring in 2018. The unique source and subaperture geometries of the profiler yield differential local jitter measurements to compute path-specific weighting functions resulting in a 30-bin profile ($L/30$ resolution). The ground station terminal was installed in an open field, and the other terminal was installed in an Airborne Aero-Optics Laboratory–Beam Control (AAOL-BC) aircraft. During data collection, the aircraft continuously orbits around the ground station for approximately 3 h flights with data collected on a per-orbit basis. The flight geometry is nominally a ground radius of 7.4 km and an altitude 2.1 km, yielding an approximately 8 km slant path. Actual geometries during flight rely heavily on cloud altitude and wind conditions. Thus exact geometries were recorded with a Trimble GPS unit installed on the aircraft.

Automated tracking software on both ends of the propagation path is necessary for data acquisition. For the ground station, the system was able to maintain track approximately 80% of each orbit with both wide field of view and narrow field of view tracking engaged. Tracking conditions on the air side were more susceptible to environmental conditions such as changes in altitude and cloud cover. The air station was able to successfully acquire and maintain track for approximately 50% of each orbit. For more detail on the tracking and data collection procedures for these flight campaigns, see Refs. [27,28].

B. Ground Station Setup

Figure 3 shows images of the ground station profiler terminal from the front and back. The terminal consisted of a 0.2032 m Meade telescope on a Meade LX200 gimbal mount. The sources (red and blue LEDs for ground station) were attached to the side, and the color SHWFS was on the back of the telescope for data collection. Additional hardware components were added to the terminal for aircraft tracking. The added components included a wide field of view (WFOV) camera for aircraft acquisition, a narrow field of view (NFOV) camera for aircraft fine-tracking, and a track beacon used by the air station for ease of tracking the ground station. The profiler terminal used the rails on the Meade telescope to maintain parallel optical axes between the telescope and LED source assembly. This experimental setup required modifications to the standard PROPS hardware. The customized terminal, depicted in Fig. 3, shows additional mounting hardware designed to keep the LED source assembly in a vertical configuration. The customized ground station terminal also included a modified beacon transmitting at 950 nm. The new beacon is detectable by the short-wave infrared track sensors on the aircraft.

C. Air Station Setup

Figure 4 shows three images: the assembly design, the profiler terminal installed in the aircraft, and an external perspective of the system.

The received light from the ground station propagated through the system as follows. Red and blue light from ground station LEDs would propagate through the atmosphere toward the aircraft, through a 30.5 cm optical window, reflect off an angled 30 cm mirror as part of the AOM360 AeroTech gimbal used for tracking, then propagate toward a 20.3 cm Celestron telescope. At the base of the telescope aperture some light would be picked off by a mirror and reflected toward a Teledyne Forward Looking InfraRed (FLIR) camera attached to a Nikon Lens, which acted as the WFOV camera for tracking. The remaining (majority) of light would be relayed through the telescope and then encounter a 50/50 beam splitter. The splitter

a) Front of terminal showing the telescope, wide field of view camera, LED sources, and track beacon

b) Back of terminal showing the telescope, narrow field of view camera, and color SHWFS

Fig. 3 Ground station profiler terminal.

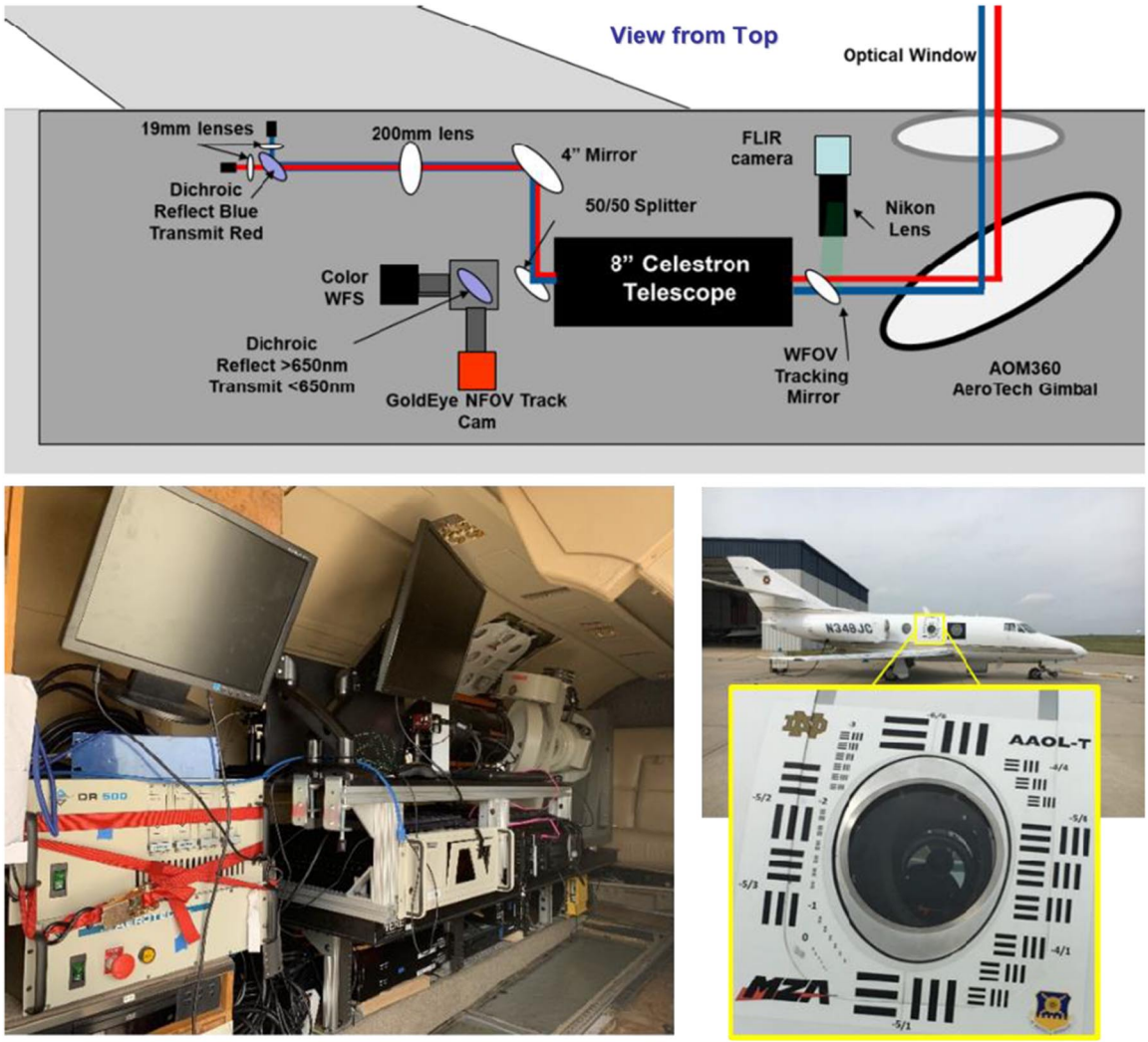

Fig. 4 Aircraft station LED source receiver, laser source emission, and tracking hardware installed in the aircraft.

sent half of the received light into the color SHWFS and the other half to the Allied Vision Technology GoldEye CL-033 NFOV track camera. The GoldEye NFOV track camera operated in the short-wave infrared range; thus the modified track beacon on the ground station terminal in Fig. 3 enabled beacon tracking for the aircraft station.

The propagation of light out of the aircraft to the ground station used laser source injection. As shown in Fig. 4, two lasers, red (637 nm) and blue (405 nm), were collimated to a diameter of 5 mm by using 19 mm lenses, and made parallel to each other with a longpass dichroic mirror. The dichroic reflected the blue laser light and transmitted the red laser light toward a 200 mm lens. After passing through the lens, the red and blue laser light entered the back of the 20.3 cm Celestron telescope (the same used for collection of ground station LED light). The combination of the 200 mm lens and 2000 mm telescope yielded a 10× magnification. Thus, the diameter of each beam was magnified to 50 mm out of the telescope with 10 mrad divergence. Out of the telescope the beams were separated vertically by 12.7 cm. After 8 km of propagation through the atmosphere, each beam was approximately 160 m in diameter. The maximum laser power was 125 mW.

IV. Aero-Optical Contamination

The theoretical construct described in Sec. II and used by the profiler in this work affords an exciting opportunity to extract turbulence parameters along a path with comparable ease relative to previous approaches. For reference, ground tests have been conducted where turbulence was reported along a path between two static profiler terminals. The successes of these ground tests led to the next step of using a profiler in an aircraft to conduct turbulence profiling experiments. However, acquiring atmospheric turbulence measurements from an aircraft has associated challenges. Namely, it was known that the turbulent boundary layer of the aircraft would introduce high-frequency optical turbulence aberrations in front of the profiler's acquisition terminal, the consequences of which were not known. Because the aero-optical boundary layer does not abide by Kolmogorov statistics, it is reasonable to wonder how the profiler's measurements may be affected. Therefore, it was beneficial to quantify the expected contamination that the boundary layer would have on these measurements. To do this, data measurements from a previous AAOL-BC campaign were used [29–32]. For these previous experiments, two aircraft were flying in close formation (≈ 50 m apart) and at high altitude (4572 m). As such, a beam propagating between these two aircraft is assumed to be subjected to negligible atmospheric distortions. The primary sources of distortions imposed onto the beam were from the naturally occurring boundary layer of the acquisition aircraft as well as the upstream propagating acoustic waves from the aircraft jet engine located downstream of the acquisition window. Therefore, by using the data collected during this close range flight experiment where negligible atmospheric distortions were imposed onto the laser beam, a C_n^2 associated with the turbulent boundary layer and acoustic contamination can be estimated. An estimate of aero-optical and aero-acoustical contamination is useful to compare with the turbulence profiling campaign results in proximity of the aircraft. This previous AAOL-BC flight campaign will be addressed as the "boundary layer (BL) campaign," for convenience. For more information pertaining to the BL campaign, see

Refs. [29–32]. To accurately compare the aero-optical and aero-acoustical environments between the BL campaign and the turbulence profiling campaign described in this work, the beam distortions measured during the BL campaign needed to be appropriately scaled to account for the data being collected at a different altitude (≈2100 m rather than 4572 m). Previous work has described the relevant scaling and properties of an aero-optical turbulent boundary layer in great detail [33]. The root mean square (RMS) of the optical path difference (OPD), $\mathrm{OPD_{RMS}}$, is often the metric used to quantify the distortions associated with an aero-optical and aero-acoustical environment. It was found that for a turbulent boundary layer, the $\mathrm{OPD_{RMS}}$ scales as

$$\mathrm{OPD_{RMS}} \approx 0.19 K_{GD} \rho_\infty M^2 \delta \sqrt{C_f} G(M) \tag{8}$$

where K_{GD} is the Gladstone–Dale constant approximated as 2.27×10^{-4} $\mathrm{m^3/kg}$ for the wavelengths used in this work, ρ_∞ is the freestream density, M is the cruise Mach number, δ is the boundary-layer thickness over the acquisition window (measured and reported in Ref. [29]), C_f is the skin friction coefficient, and $G(M)$ is a function that, for this environment, can be approximated as 1. For greater detail on the development, assumptions, and limitations of Eq. (8), see Ref. [33]. For the BL campaign environment, an $\mathrm{OPD_{RMS}}$ from the aircraft turbulent boundary layer is expected to be ≈0.0123 μm based on Eq. (8). In practice, the overall measured $\mathrm{OPD_{RMS}}$ during the BL campaign at Mach 0.4 was found to be 0.052 μm. It has been shown that the upstream propagating acoustic waves from the jet engine introduce appreciable beam distortions. The contributions to $\mathrm{OPD_{RMS}}$ from both the boundary layer and the acoustics can be decoupled using dispersion analysis, as described in great detail in Ref. [31]. With this, it was shown that the boundary layer had an $\mathrm{OPD_{RMS_{BL}}}$ of ≈0.0356 μm and the acoustic contamination had an $\mathrm{OPD_{RMS_{Acoustics}}}$ of ≈0.0339 μm. It is worth noting that the measured turbulent boundary layer $\mathrm{OPD_{RMS}}$ is slightly higher than what is predicted by Eq. (8) for the altitude of data collection during the BL campaign (≈0.0123 μm). The increased energy of the AAOL-BC turbulent boundary layer is most likely attributed to a vortical structure that originates at a cavity in the pilot's window and propagates downstream over the acquisition window. This turbulence structure causes the boundary layer of the aircraft to slightly deviate from a canonical description. Nevertheless, by using the measured boundary layer $\mathrm{OPD_{RMS}}$ of ≈0.0356 μm with Eq. (8), the $\mathrm{OPD_{RMS_{BL}}}$ can be altitude scaled to match the environment where turbulence profiling measurements were collected in the campaigns emphasized in this paper. Using the appropriate freestream density and kinematic viscosity (embedded in the skin friction calculation) for a standard atmosphere at an altitude of 2100 m, the boundary layer during the turbulence profiling campaign was expected to have an $\mathrm{OPD_{RMS_{BL}}}$ of ≈0.0458 μm. Because the profiler's terminal also sees a contribution to beam distortions due to acoustics, it was also necessary to reintroduce this contamination factor. In Ref. [31], it was shown that the $\mathrm{OPD_{RMS}}$ due to acoustics stays approximately the same regardless of the flight conditions. Therefore, the boundary layer and the acoustic contributions to $\mathrm{OPD_{RMS}}$ can be combined for a scaled $\mathrm{OPD_{RMS}}$ using

$$\mathrm{OPD_{RMS_{Scaled}}} = \sqrt{(\mathrm{OPD_{RMS_{BL}}})^2 + (\mathrm{OPD_{RMS_{Acoustics}}})^2} \tag{9}$$

This value for $\mathrm{OPD_{RMS_{Scaled}}}$ estimated the strength of the aero-optical and aero-acoustical environment near the aircraft during the turbulence profiling campaigns.

This $\mathrm{OPD_{RMS_{Scaled}}}$ was then used to estimate a C_n^2. Although C_n^2 is not common language in the aero-optics community, extracting a C_n^2 in this fashion is useful for quantifying the contamination that may be registered through the profiler due to the aerodynamics of the aircraft. To do this, the tilt-removed phase variance of the measured laser beam is used. The tilt-removed phase variance or higher-order phase variance [25] σ_{HO}^2 is related to the aperture diameter D and atmospheric coherence length r_0 by

$$\sigma_{\mathrm{HO}}^2 = 0.134\left(\frac{D}{r_0}\right)^{5/3} \tag{10}$$

By using the $OPD_{RMS_{\mathrm{Scaled}}}$ (comprising the scaled boundary layer and acoustic contamination), a tilt-removed phase variance of 0.4532 $\mathrm{rad^2}$ was calculated. Consequently, an r_0 of 9.63 cm was extracted. With the relation

$$r_0 = 1.68(C_n^2 L \kappa^2)^{-3/5} \tag{11}$$

r_0 can be used to calculate C_n^2 [7]. In this equation, κ is the laser wavenumber, and L is the propagation range. The propagation range was taken to be the size of the bin for the profiler ($L/30$), which was approximately 267 m. As such, a C_n^2 value of 3.16×10^{-15} $\mathrm{m^{-2/3}}$ was calculated. Later on, this value is compared with the measured profiles to show whether the profiler measurements reveal a similar degree of contamination from the boundary layer and acoustic environment in C_n^2 values closest to the aircraft.

V. Turbulence Measurements and Atmospheric Model Comparison

The profiler measurements provided the C_n^2 values along the optical propagation path. For every SHWFS data sequence that passed the filtering process, a 30-bin solution is outputted where each bin corresponds to approximately 267 m of propagation path. Each terminal naturally generates its own single-sided profile solution. To get a double-sided profile, the profile solution must be computed from the simultaneously collected sets of DDTV measurements from air and ground terminals. The double-sided solution used the path weighting functions from both ends, which resulted in full path sensitivity. The measured double-sided solutions are compared with the traditional Hufnagel-Valley 5/7 (HV57) model [6,34], as well as the state-of-the-art Laser Environmental Effects Definition and Reference (LEEDR) weather cube atmospheric model [35–37]. The following subsections describe how double-sided solutions are calculated, how the aerocontamination of the atmospheric profiler is removed, and how the measurements compared with atmospheric models.

A. Double-Ended Profile Generation and Results

Because of the relative source separation distance (≈15 cm) versus farthest subaperture separation distance (≈19 cm), single-sided profiles only provide DDTV weighting functions on the side of the propagation path closest to the receiver. Single-sided profiles are independently generated for both the air and ground station. Data collected by the air station resolves the portion of the path closest to the aircraft, whereas the ground station resolves the lower half of the propagation path. Double-sided profiles are generated by using time-synced statistics from both stations, allowing the weighting functions to more accurately resolve the entirely of the path. The quality of SHWFS data determines which pairs of subapertures are used in the DDTV algorithm. Thus, the SHWFS data also drive which weighting functions are used in the profiling solution. The profiling solution algorithm iterates until convergence.

Turbulence profiling results obtained from the profiling campaign are shown in Fig. 5. Here, C_n^2 is plotted versus altitude above ground level for different orbits, and the data lines on each plot correspond to measurements that took place at different times within each orbit (data recorded between 9:28 a.m. and 10:12 a.m. on August 29, 2019). For comparison, the widely used HV57 model is also plotted in green. It can be seen that at the ground, the empirical data and HV57 model are in agreement. However, the measured values show that C_n^2 decreases from 1×10^{-14} to 1×10^{-16} $\mathrm{m^{-2/3}}$ about 100 m off the ground, whereas HV57 predicts a more gradual decrease in turbulence strength with altitude.

In general, HV57 tends to overpredict the turbulence strength at low altitudes. Interestingly, at the highest altitude corresponding to the data collected next to the aircraft (altitude above ground level ≈2000 m), there exists a seemingly spurious spike in turbulence

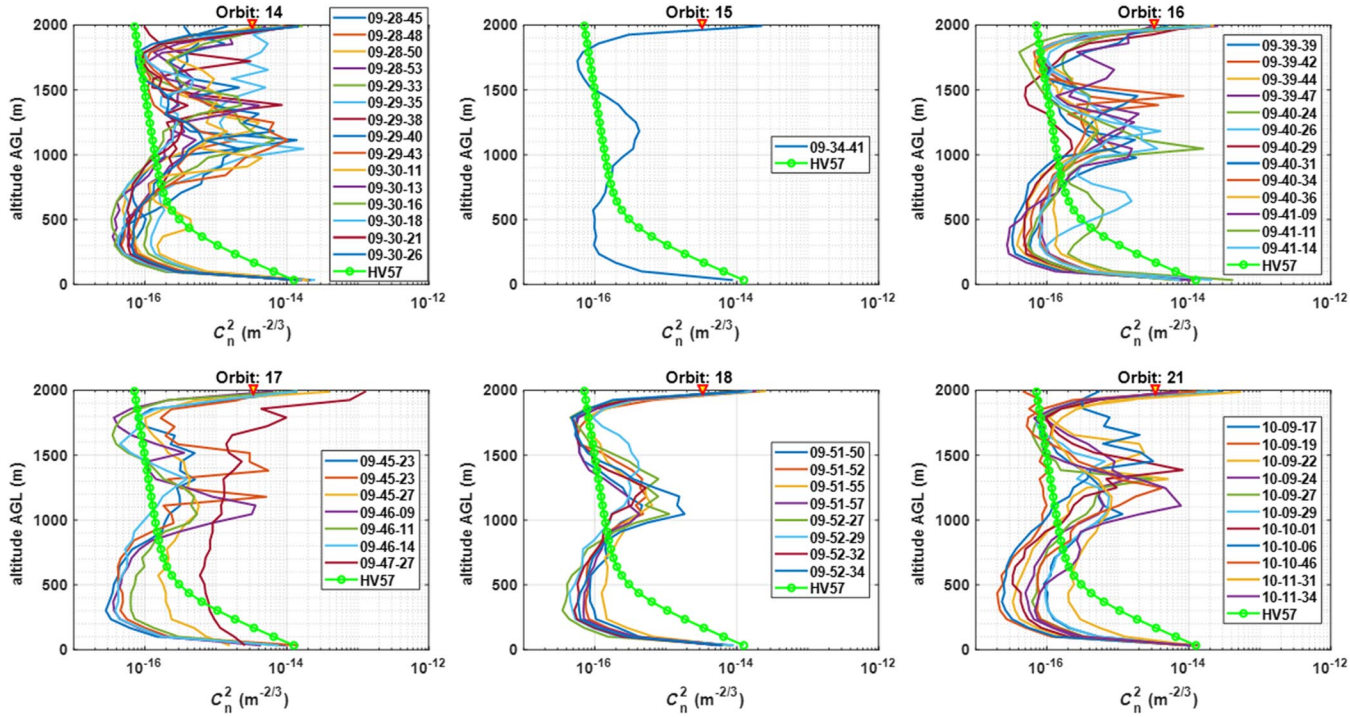

Fig. 5 Profiling results for various orbits between 9:28 a.m. and 10:12 a.m.

strength. Current atmospheric models do not predict a drastic rise in turbulence intensity at these altitudes like what is seen in the measured data. The aerodynamic turbulence associated with the aircraft boundary layer imposes localized distortions onto the incoming light in front of the receiving aircraft profiler terminal. Therefore, the spikes in optical turbulence strength seen above approximately 1750 m are not believed to be attributed to atmospheric turbulence; rather, they are due to aero-optical and aero-acoustical effects in proximity to the aircraft acquisition window. These measured bins closest to the aircraft very closely match the predicted level of boundary layer and acoustic contamination described in Sec. IV. In Fig. 5, the predicted aero-optical contamination C_n^2 value from Sec. IV of 3.16×10^{-15} m$^{-2/3}$ is depicted at 2000 m altitude above ground level as a red triangle.

For comparison, a measured double-sided turbulence profile for a ground-to-ground traverse is shown in the left plot of Fig. 6. There was no significant change in terrain or altitude, which correspondingly produces a turbulence profile that remains fairly constant across the path. It is clear that the phenomenon seen in the air to ground experiments is not present here. The right plot of Fig. 6 highlights this aero-optical induced contamination. The contamination is isolated in the first 2–3 bins nearest to the aircraft. A key advantage of using a DDTV-based algorithm is that it allows the nonatmospheric optical disturbances, which in this case includes the aero-optical and aero-acoustical contamination, to be removed. This will be discussed in greater detail in the next section. Also seen in the air-to-ground turbulence profiles of Fig. 5 is a significant increase in C_n^2 between 1000 and 1500 m altitude above ground level, where HV57 seems to underpredict turbulence strength. It is difficult to make conclusive statements about the reasons for the turbulence enhancement between 1000 and 1500 m altitude above ground level, but one reasonable hypothesis is that the measurements are capturing the turbulence effects at the top of the Earth boundary layer [38,39]. This spike in C_n^2 is followed by a decay in turbulence strength that

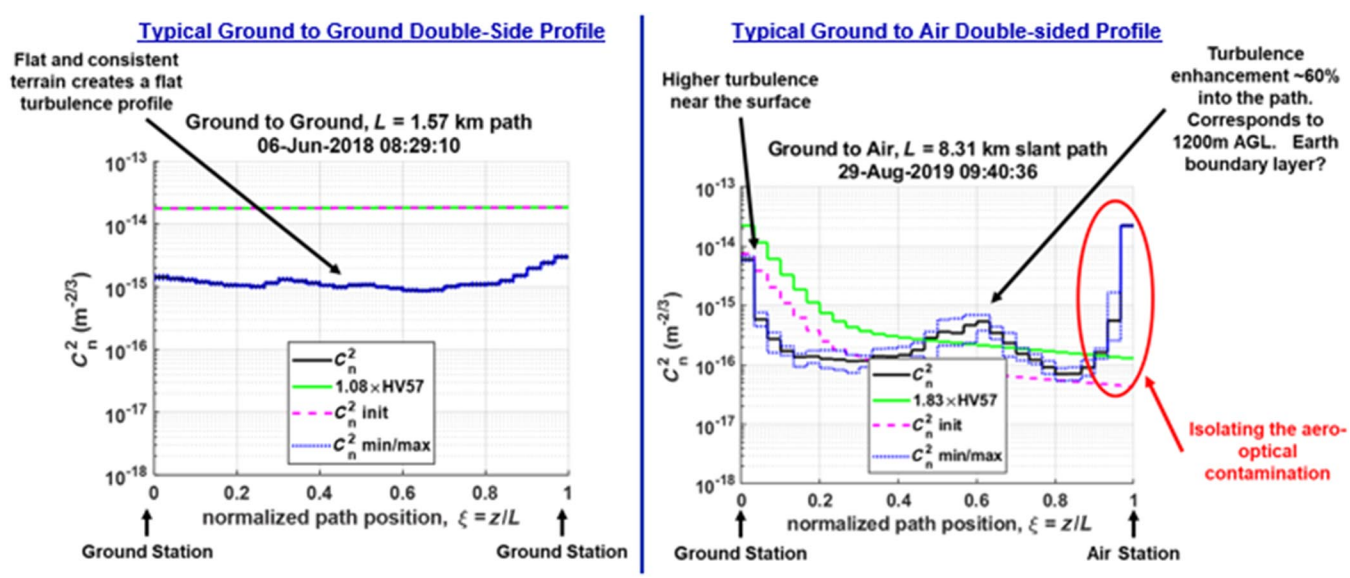

Fig. 6 Comparison between a typical ground-to-ground (G2G) profile versus a ground-to-air (G2A) profile.

converges to a value in agreement with HV57 between altitudes of 1500 and 1700 m.

B. Removing Aero-Optical Contamination

Aero-optical contamination is removed by omitting the affected bins. An illustrative example of this process is shown in Fig. 7. The two plots each show the measured C_n^2 profiles as a function of altitude from a single orbit. The x axes show a logarithmic scale of C_n^2, and the y axes are linear-scale altitude above ground level. Figure 7a contains the raw profiles with the contamination and the HV57 profile (green) modeled from the path geometry. Each raw profile is labeled with a timestamp representing the time when the data were collected. Because HV57 is only altitude dependent and the aircraft altitude did not significantly fluctuate during the orbit, there is a single model profile curve. Similar to the observations in Fig. 6, Fig. 7a shows the apparent consistency in profiles near ground level and bumps in C_n^2 from 900 to 1400 m altitude above ground level. Turbulence dips in magnitude around 1500 m for nearly all the measured profiles. After the dip is another bump in turbulence from 1800 to 2000 m altitude above ground level. These high-altitude bumps are the result of aero-optical contamination from the aircraft, as discussed above. Figure 7b is a statistical summary illustration of the results for the same orbit; however, the contaminated bins are now removed, as shown by the lack of measured data above 1800 m. Figure 7b illustrates the same measured profiles from Fig. 7a, but plotted as a mean in solid black and min/max as dotted blue lines. By omitting the contaminated bins, the measurements and modeled atmospheric profiles are more directly comparable. Also illustrated in Fig. 7b are LEEDR model profiles [35–37] computed for times surrounding the orbit time, 09:00 in green and 10:00 in cyan.

The LEEDR model takes in numerical weather prediction data to generate a 3D atmospheric model. Specifically, the LEEDR models shown in Fig. 7b are generated using a particular kind of numerical weather prediction data, referred to as high-resolution window (HIRESW). The HIRESW data come from regional weather research and forecasting models. These data are provided on a 5 km uniform grid and spans 0–10 km altitude above ground level. Because the LEEDR profiles are path and terrain dependent, there are multiple profiles per orbit. Each modeled profile is dependent on the geometries and terrain underneath the propagation path along the orbit. Figure 7b is illustrating the mean curve for the 09:00 and 10:00 HIRESW sets. At surface level, Fig. 7b shows that the LEEDR model and measured C_n^2 profiles have similar magnitudes. Additionally, the bumps in turbulence from 900 to 1400 m captured by the profiler are also apparent in the weather cubes. Generally, the measured profiles have similar shape to the LEEDR model.

In Fig. 7b, the magenta and red lines in the plot are the HV57 model profiles calculated with and without an α multiplier, respectively. The α multiplier is derived from the average of the measured coherence diameter r_0^{PROPS} for each profile and calculated HV57 coherence diameter r_0^{HV57} for the path geometry. This α multiplier is written as

$$\alpha = \left(\frac{r_0^{\mathrm{PROPS}}}{r_0^{\mathrm{HV57}}}\right)^{-5/3} \tag{12}$$

and it scales the HV57 model profile so its r_0 matches the measured r_0. Here, r_0^{PROPS} is defined as

$$r_0^{\mathrm{PROPS}} = \frac{r_0^A + r_0^B}{2} \tag{13}$$

Figure 7b shows that the average contamination-removed profiles in orbit 14 roughly agree in shape with the LEEDR weather profiles from surface level to 1000 m altitude above ground level. Beyond 1000 m the average measured profiles match very well with the LEEDR weather cubes.

The measured profiles are typically analyzed on a normalized path position plot. Figure 8 presents an alternative visual representation of the measured C_n^2 profiles with and without the aero-optical contamination. Here, logarithmic C_n^2 is plotted as a function of normalized path position.

On the x axis, the zero-position is the air terminal and the one-position is the ground terminal. Plots (a) and (b) show a single measured profile with and without aero-optical contamination, respectively. The red line illustrates the normalized path position each bin represents, whereas the black line simply connects the centers of each bin. Also shown in green is the reference HV57 model. Turbulence strength at the ground terminal (x axis equals 1) is similar to HV57, but measurements indicate that turbulence falls off with slant-path range significantly faster than modeled. Additionally, the measured bump in turbulence about 40% into the path from the air perspective is not captured by the model. With aero-optical contamination removed, as shown in plot (b), the turbulence characteristics near the air station are more consistent with expectation and model, indicating the importance of isolating those bins. Plots (c) and (d) in Fig. 8 contain all measurements for a single orbit with and without aero-optical contamination, as well as HV57 plotted in green for reference. The predicted aero-optical contamination C_n^2 described in Sec. IV is shown as a red triangle. These results show the same trend as in Figs. 8a and 8b. The ground terminal model and measurements are in agreement, but measurements indicate turbulence falls off faster than modeled. The characteristic bump 40% into the path from air perspective is still evident. The spike in turbulence close to the air terminal is consistent in all profiles.

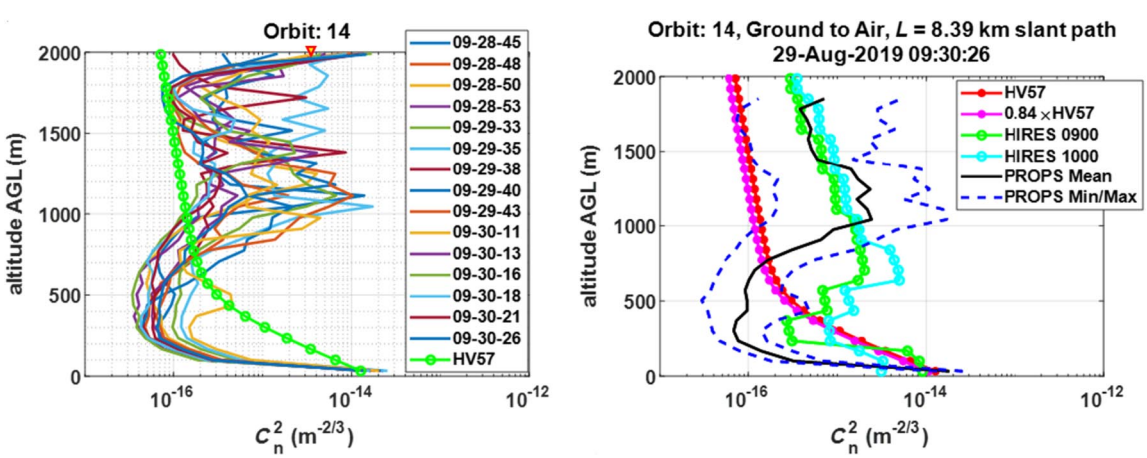

a) Measurements within one orbit

b) Measurements statistic for one orbit

Fig. 7 Eliminating the profile bins closest to the aircraft reduced the aero-optical contamination of the atmospheric profile measurements and enables a direct comparison to C_n^2 modeling.

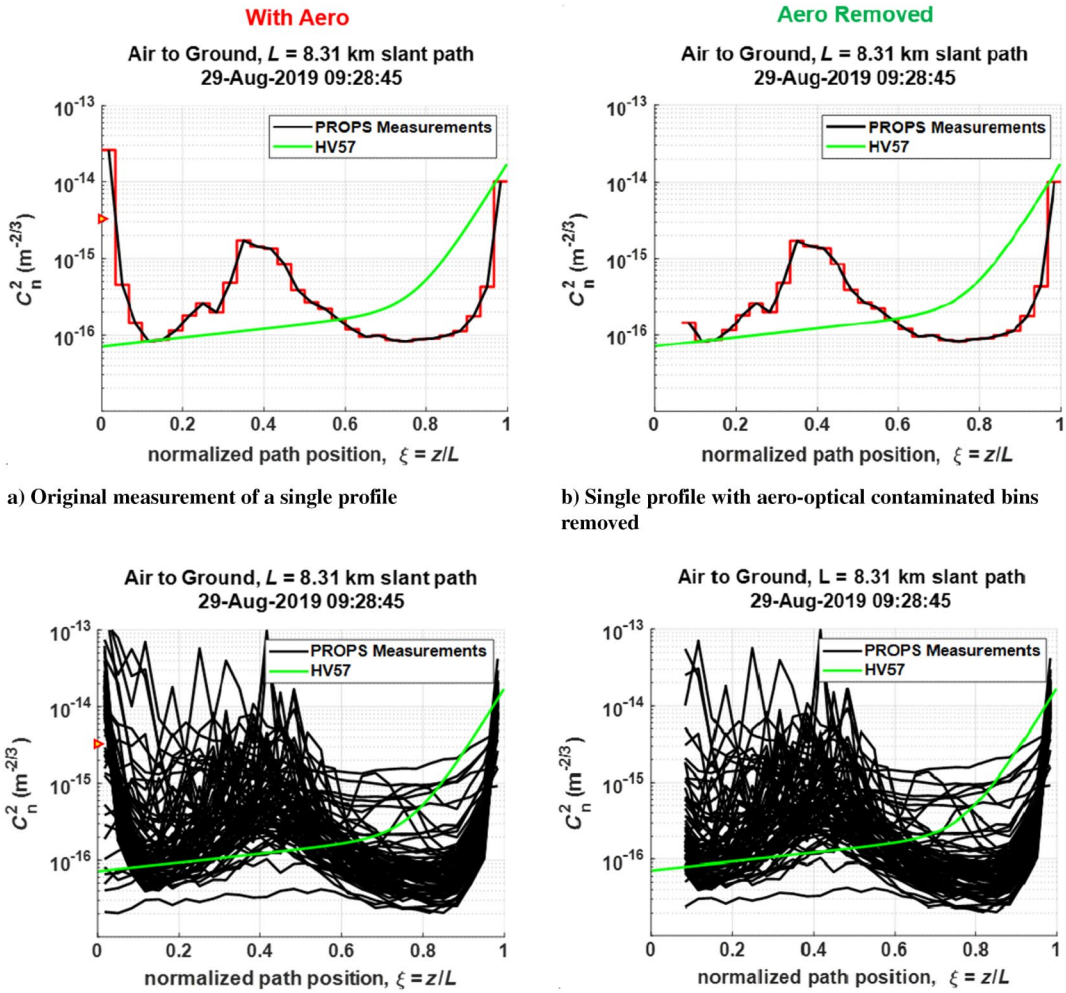

a) Original measurement of a single profile

b) Single profile with aero-optical contaminated bins removed

c) Original measurements with aero

d) All measurements aero-optical contaminated bins removed

Fig. 8 The aero-optical contamination can appear as high C_n^2 values in the profile bins closest to the aircraft.

C. Spatial Comparison of Measurements Versus Modeling

A unique aspect of this data collection is the varying terrain and geometries at ground level below the orbital path of the aircraft. The measurements versus modeling analysis is summarized by comparing the spatial representation of an ensemble of measurements to the turbulence models generated for that time. Figures 9a–9c show the HV57 profile, a LEEDR weather cube profile, and measured profiles, respectively.

The C_n^2 strength is represented by the color of each bin. The color bar is on a logarithmic scale. Red indicates the strongest turbulence, C_n^2 of 1×10^{-13} m$^{-2/3}$, and blue indicates the weakest turbulence, C_n^2 of 1×10^{-17} m$^{-2/3}$. Because HV57 is only dependent on altitude, the profiles around the orbit are identical as seen in Fig. 9a. The 10:00 LEEDR weather cube generated from HIRESW numerical weather prediction data in Fig. 9b is dependent on terrain so there are slight variations in each spoke, but over relatively short distances the differences are minimal. There is a strong contrast between Figs. 9a and 9b. HV57 models turbulence that is much stronger at the ground station (center of the spokes) and falls off quickly with altitude. However, LEEDR models turbulence at medium strength (approximately 1×10^{-15} m$^{-2/3}$) over the entire propagation path with an enhancement about 30% into the path from ground terminal to air terminal. Figure 9c contains all double-ended profiler measurements over the course of the one hour of flight. The aero-optical contamination is apparent as the orange-red bins at the edge of the spokes. Like HV57, but unlike LEEDR, measurements indicate strong turbulence at the ground terminal (center of spokes). Measurements show that turbulence near the surface decreases rapidly with increasing altitude. Then, turbulence begins to increase again several hundred meters above the ground, which is possibly due to the Earth boundary layer. The LEEDR model in Fig. 9b captures a turbulence enhancement in the path as well, indicated by the orange ring. Overall, the spatial comparison of profiler measurements reveals interesting similarities and differences in the characteristics between measurements and modeling. These measurements will be used to further enhance the modeling capabilities.

VI. Modeling and Measurements Extended to System Performance

Up to this point, the analysis focuses on comparing double-ended profiler measurements with HV57 and LEEDR atmospheric models. This section extends the analysis by examining directed energy system performance analysis for an aircraft system looking down and for a ground system looking upward. The comparison of air-to-ground engagements versus ground-to-air engagements will use realistic directed energy system parameters with a 30 cm aperture operating a 1 MW and 1 μm laser.

A. System Performance Modeling with and Without the Aero-Optics

Both atmospheric conditions as well as an aero-optical environment impact the performance capability of a directed energy system. Atmospheric optical turbulence is caused by total temperature variations in the atmosphere. Aero-optical effects, on the other hand, are optical distortions imposed on a laser beam due to a varying density

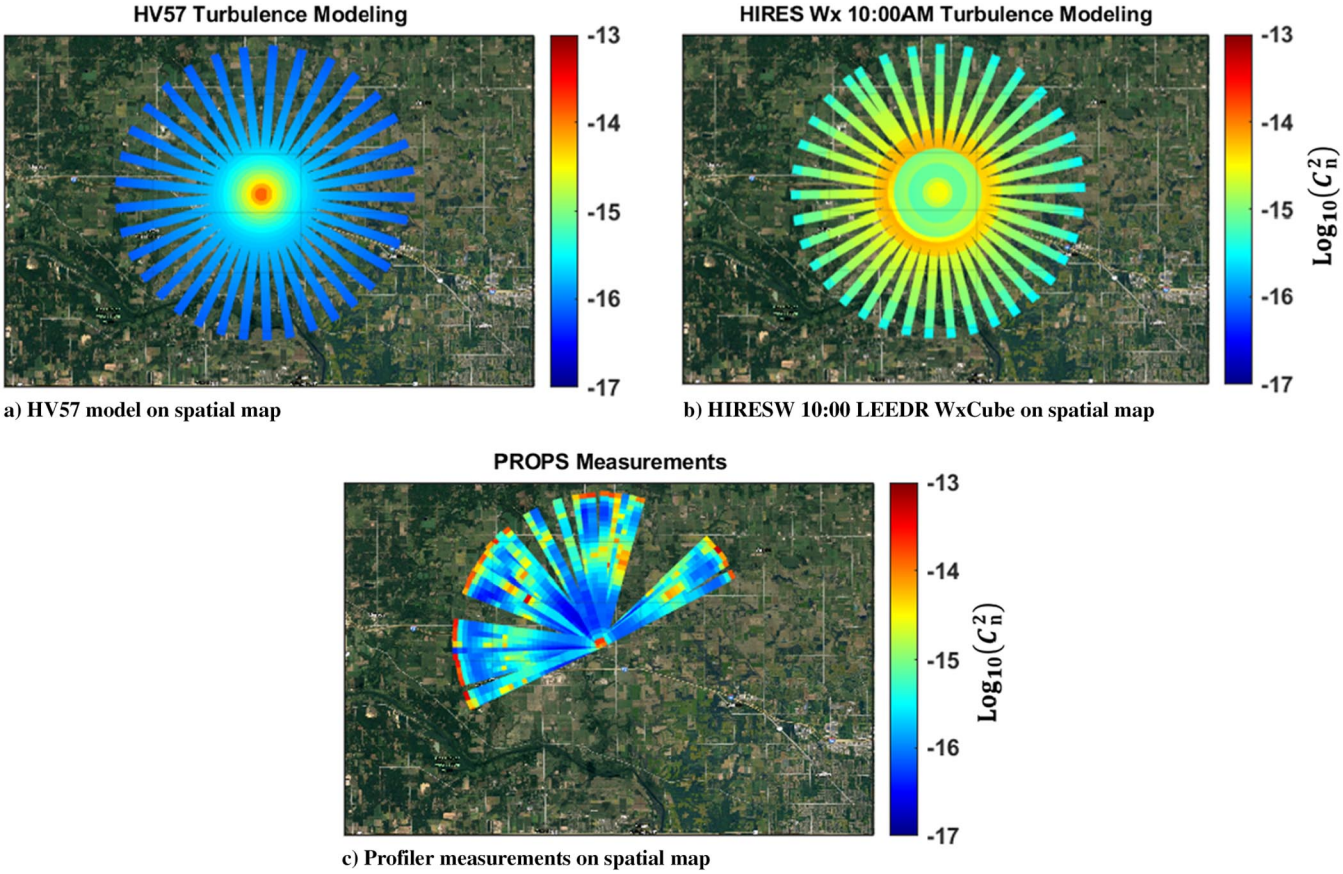

a) HV57 model on spatial map

b) HIRESW 10:00 LEEDR WxCube on spatial map

c) Profiler measurements on spatial map

Fig. 9 Compare modeling and measurements on a spatial map of the experiment site.

field around an aircraft, caused by either compressibility effects at flight Mach numbers above 0.3 or by pressure variations [1,40–42]. The physical cause of aero-optical effects is fundamentally different from atmospheric optical effects.

This section presents system performance modeling as a function of the measured C_n^2 profile. The analysis focuses on capturing differences in performance with and without the inclusion of aero-optical contamination. Removal of the two bins closest to the air terminal allows for a better understanding of how atmospheric optical turbulence alone impacts system performance. Leaving the aero-optical contamination in the data set allows the error associated with these disturbances to be assessed. In the following figures, measured and modeled system quantities are presented with and without the aero-optical contamination. Then, using these measurements and modeled quantities (with HV57 and LEEDR), the system performance is computed. Figure 10 compares four system parameters (spherical Rytov number, isoplanatic angle θ_0, Greenwood frequency, and Tyler frequency) between results with and without aero-optical contamination. Each plot contains profiler measurements, LEEDR weather cube (in blue), and HV57 model (in green). The hourly temporal resolution of LEEDR results in lulls in this model's results. First, in Figs. 10a and 10b, spherical Rytov number is analyzed. Generally, the removal of aero-optical contamination does not yield significant differences in Rytov number. The clustering of measurements between each plot is similar, and magnitude differences are minimal. Rytov is most sensitive to the turbulence in the middle of the propagation path and the midpath conditions do not change between Figs. 10a and 10b. The only differences in the turbulence profile are in the bins closest to the aircraft where Rytov has minimal sensitivity. The Rytov number computed from the profiler measurements has more agreement with the HV57 model than the LEEDR model. In Figs. 10c and 10d, isoplanatic angle θ_0 is not affected by the removal of aero-optical contamination. θ_0 is sensitive to turbulence deep into the path. Thus, for an air-to-ground (A2G) system, the removal of the first two bins nearest to the aircraft does not have much impact on the θ_0 measurements. Generally, the HV57 and LEEDR models underestimate the measured isoplanatic angle. The measured and modeled Greenwood frequencies are presented in Figs. 10e and 10f. The removal of the aero-optical contamination significantly influences the results. With contamination, many of the measurements are around 200 Hz, but without contamination those same measurements fall to around 100 Hz. Several measurements are originally over 700 Hz, but without contamination, the magnitudes are significantly lower and more closely align with the HV57 model. This is expected because the boundary layer of the aircraft introduces higher-order aberrating structures. The Tyler frequency, presented in Figs. 10g and 10h, is influenced similarly. The Tyler frequency measurements are mostly halved due to the removal of the aero-optical contamination. Similarly, the Tyler frequency measurements are more consistent with the HV57 model and LEEDR model. The Greenwood frequency and Tyler frequency are computed from the C_n^2 profile and wind profile. Therefore, by removing the aero-optical contamination, the magnitude of the C_n^2 and wind profiles are reduced. Consequently, the Greenwood and Tyler frequencies also significantly decrease when those bins are removed.

These optical parameters can be extended to system performance parameters. Figure 11 compares system performance parameters (spherical coherence diameter r_0, open-loop jitter, and open-loop Strehl) for the same air-to-ground system between results with and without the aero-optical contamination. The top row contains results with aero-optical contamination and the bottom row contains results without contamination. Each of these performance measurements change significantly with the removal of aero-optical contamination. Beginning with coherence diameter r_0 in Figs. 11a and 11d, the removal of aero-optical contamination results in significantly larger values for many of the measurements. This result is expected because the bins closest to the aircraft impose a turbulence enhancement, which naturally will result in a smaller r_0 value. With contamination, r_0 is more consistent with the sparse LEEDR modeling than the

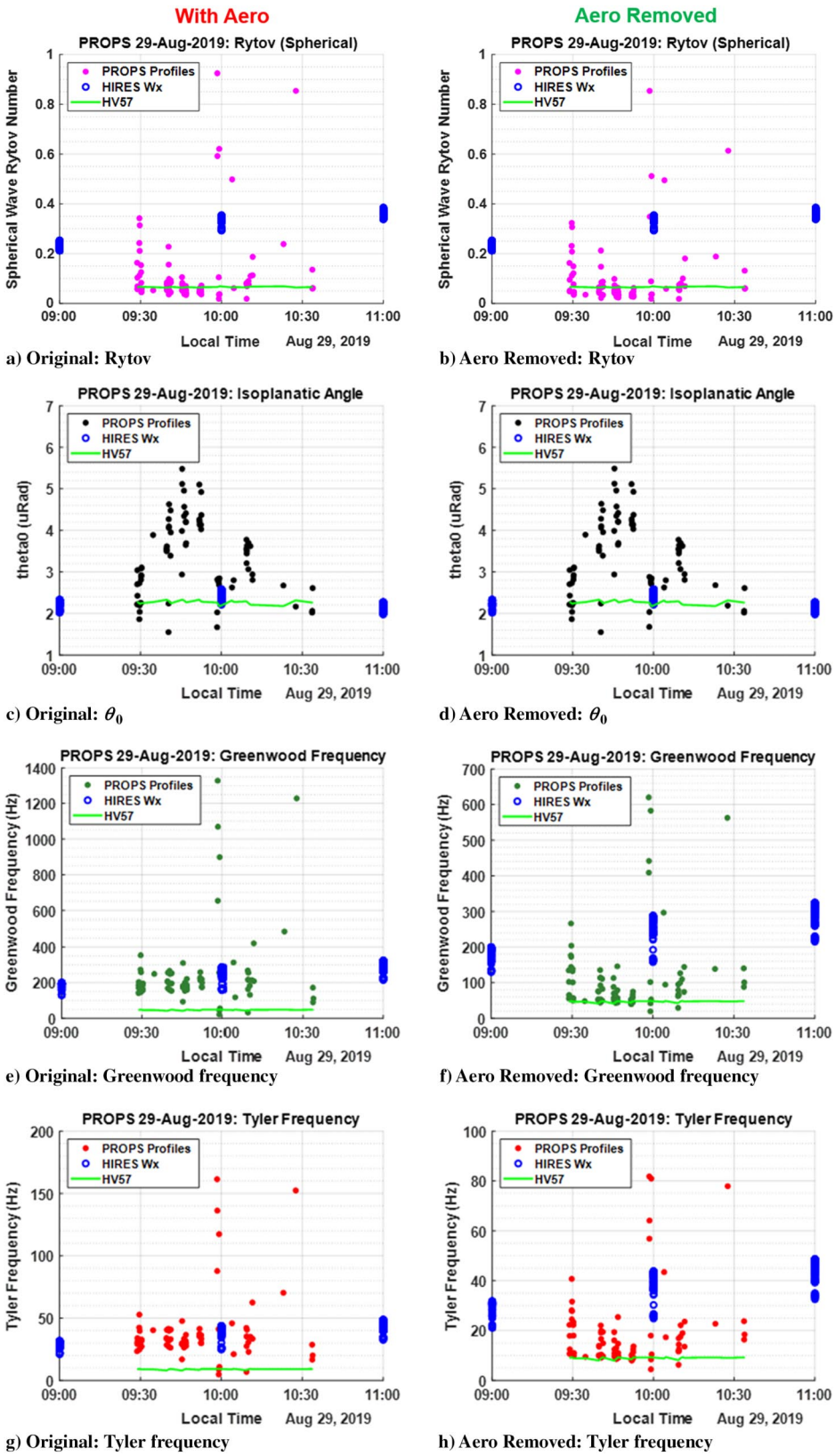

Fig. 10 System performance parameters with and without aero-optical contamination.

HV57 model. The r_0 measurements with the aero-optical contamination removed are less clustered but are in closer agreement with the HV57 model results. Figures 11b and 11e show atmospheric open-loop jitter that mostly decreases with the removal of aero-optical contamination. Originally, the measurements are clustered more around the LEEDR model, but with contamination removal the open-loop jitter values become clustered closer to the HV57 model. Figures 11c and 11f present open-loop Strehl with and without tilt removal. The measured open-loop Strehl significantly increases when aero-optical contamination is removed. Many of the tilt-removed Strehl measurements (red points) are clustered around HV57 tilt-removed Strehl.

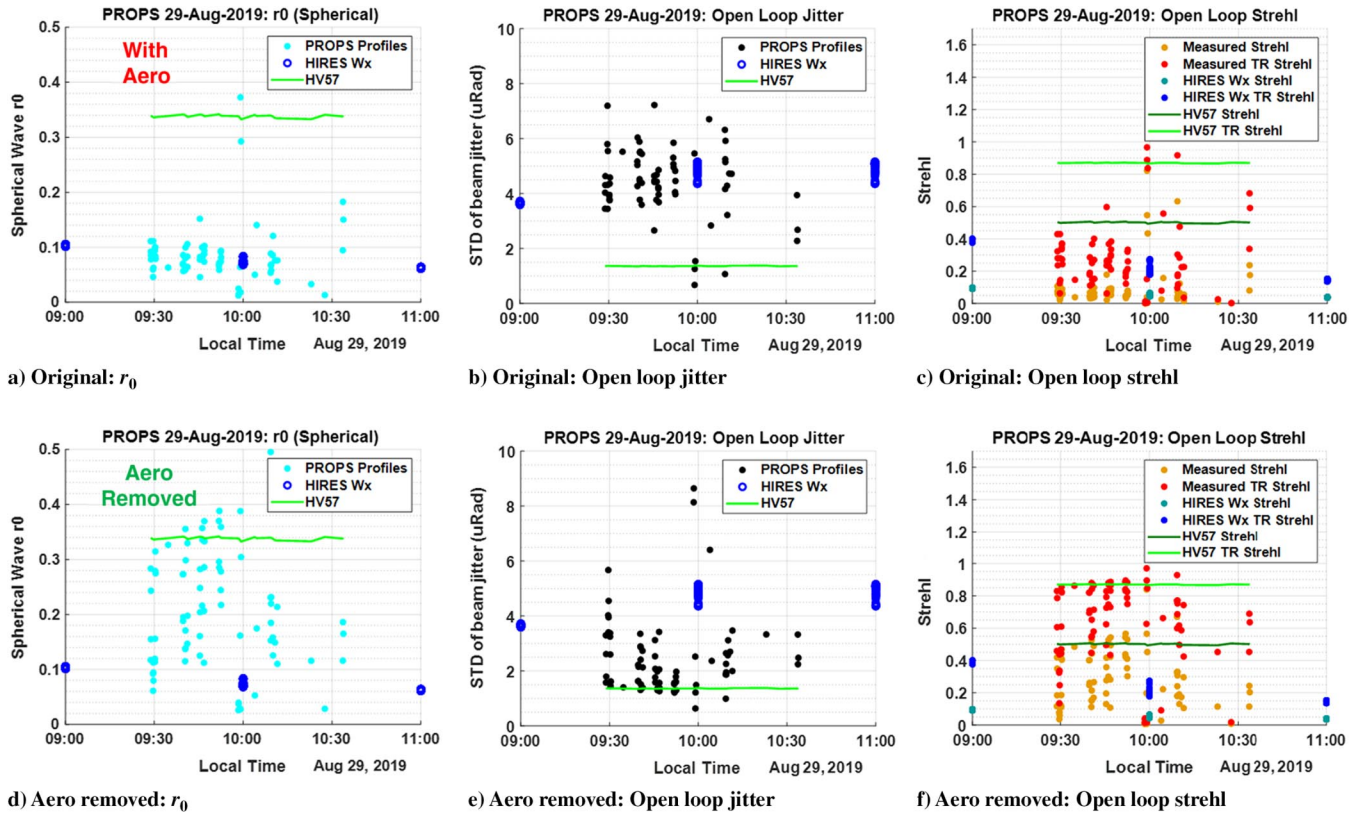

a) Original: r_0 b) Original: Open loop jitter c) Original: Open loop strehl

d) Aero removed: r_0 e) Aero removed: Open loop jitter f) Aero removed: Open loop strehl

Fig. 11 System performance parameters with and without aero-optical contamination.

B. System Performance Modeling Comparison Between Air-to-Ground and Ground-to-Air

This section presents a comparison of system measurements and modeling between air-to-ground and ground-to-air engagements. All results in this section are free from aero-optical contamination, so some of the air-to-ground plots are identical to air-to-ground "Aero Removed" results presented in the previous section, Sec. VI.A. For slant path engagements, the system performance and system capabilities will drastically differ between up-looking systems versus down-looking systems. Figure 12 compares air-to-ground (left column) and ground-to-air (right column) measurement parameters: spherical wave Rytov number, isoplanatic angle, Greenwood frequency, and Tyler frequency. Like before, each plot contains three sets of data: profiler measurements, LEEDR weather cube models from high-resolution window data, and HV57 model. Plots (a) and (b) confirm that Rytov weighting function is symmetric between each terminal. For a particular turbulence profile, Rytov number does not change between an air-to-ground and ground-to-air system. Plots (c) and (d) compare isoplanatic angle θ_0. It can be seen that there is a pronounced difference between air-to-ground and ground-to-air system. The measured isoplanatic angles from ground-to-air are generally higher than air-to-ground, as expected. Because θ_0 is sensitive to turbulence out in the path, an air-to-ground system observes smaller isoplanatic angles than an up-looking ground-to-air system. Plots (e) and (f) show the same Greenwood frequency results from each terminal. This symmetry is expected because Greenwood frequency is derived from C_n^2 and wind profiles. If the measurement is made from one terminal, the results are the same as from the other terminal because the C_n^2 and wind profiles reverse orientation, yielding the same data for the calculation of Greenwood frequency. For the same reason, plots (g) and (h) show the same Tyler frequency results from each terminal.

Furthermore, the optical parameters can be extended to other system performance metrics. The results are obtained using the same example system with a 30 cm aperture operating at wavelength of 1 μm . Figure 13 shows the system performance modeling parameters (spherical wave r_0, open-loop jitter, and open-loop Strehl) for a ground engagement. It is apparent that the models are pessimistic, showing r_0 values that are generally lower than measurements. While the HV57 and LEEDR models forecast r_0 to be approximately 6 cm, the profiler measurements show r_0 values ranging from 5 to 15 cm. The open-loop jitter plot in the center of Fig. 13 shows a similar performance trend. Open-loop jitter is a function of r_0 and inversely proportional [43,44]. The modeling shows a standard deviation of beam jitter to be 5–6 μrad. However, the measurement mostly reported open-loop atmospheric jitter under 5 μrad. For context, the tracking terminal at the ground station described in Sec. III had two optical tracking systems (acquisition track system and fine track system). The instantaneous field of view of the acquisition track system, which provided the wide field of view, was set to 62.7 μrad, and the instantaneous field of view of the fine track system, which provided the narrow field of view, was set to 1.65 μrad.

For a ground-to-air system with similar instantaneous field of views, the jitter created by uncompensated atmosphere shown in Fig. 13 is a small fraction of a pixel in the acquisition track system and 2–4 pixels in the fine track system. In those terms, the HV57 and LEEDR model's forecast anticipates around 4 pixels of atmospheric jitter; however the measurements indicated an observed 2–4 pixels throughout the data collection. Similarly, Fig. 13 also shows the open-loop Strehl ratio (right). The Strehl ratio and tilt-removed Strehl are also a function of r_0 [45]. This plot contains several key trends. First, for a ground-to-air system, the strongest turbulence along the propagation path is near the aperture, and therefore the Strehl ratio is relatively small. Second, the HV57 model and LEEDR model are in agreement and indicate a Strehl of approximately 3–5%. The profiler measurements show the Strehl varying from 2 to 16%. Third, by removing the tilt, the Strehl ratio significantly increases. The tilt-removed values are representative of having an ideal fast steering mirror in the system that corrects for the tilt disturbances. The tilt-removed values, indicated in Fig. 13 by "TR," are 10–15% for the models and 10–60% for the profiler measurements. Lastly, as observed in previous plots, the LEEDR model does not have the temporal resolution to capture trends occurring at the minute-by-minute scale. Overall, the models tend to be underrating the ground-to-air system performance measurements.

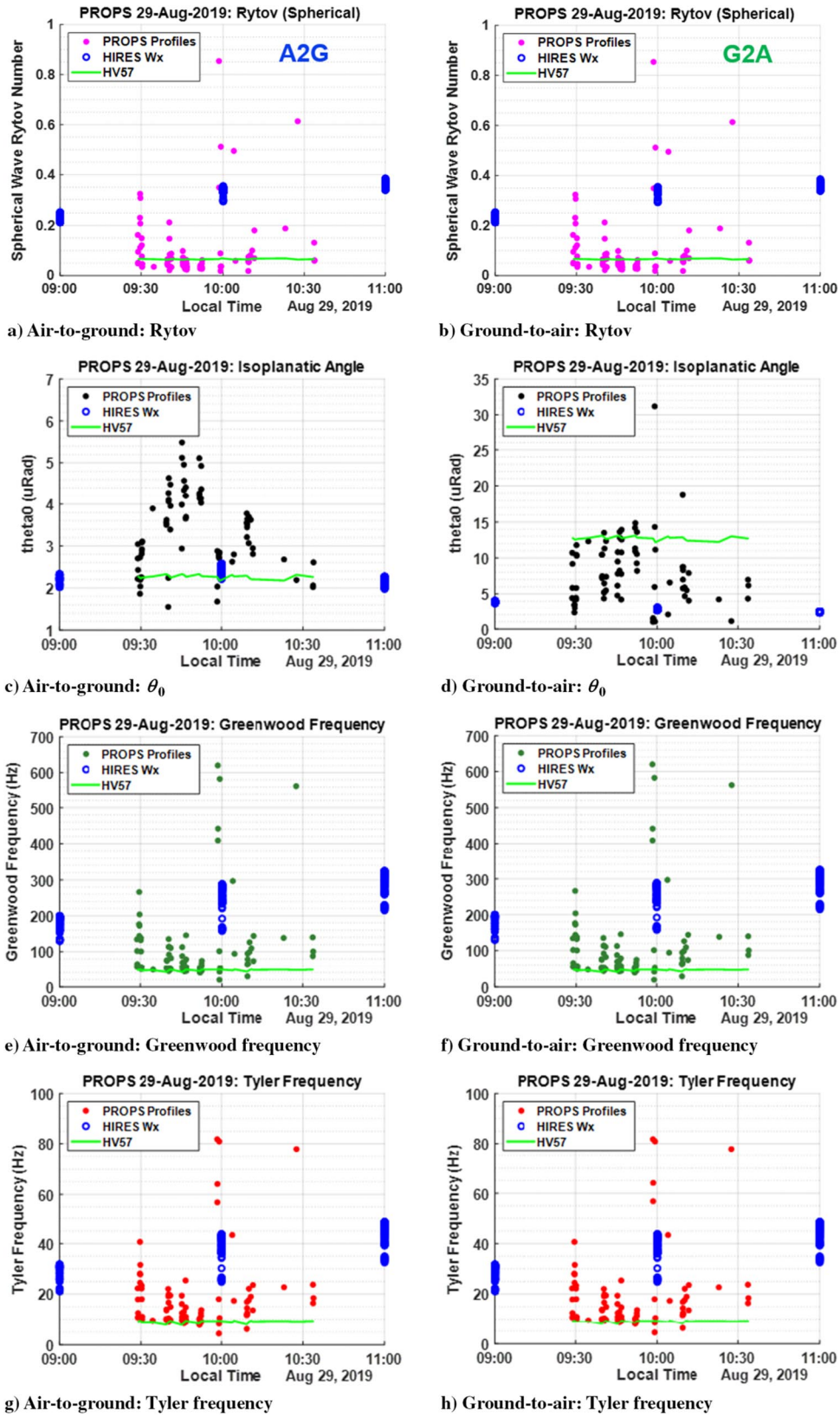

a) Air-to-ground: Rytov

b) Ground-to-air: Rytov

c) Air-to-ground: θ_0

d) Ground-to-air: θ_0

e) Air-to-ground: Greenwood frequency

f) Ground-to-air: Greenwood frequency

g) Air-to-ground: Tyler frequency

h) Ground-to-air: Tyler frequency

Fig. 12 Air-to-ground vs ground-to-air system performance parameters without aero-optical contamination.

In a similar way, the system performance can be modeled using the same system parameters and the same turbulence profiles, but with a reversed operation geometry. Figure 14 shows air-to-ground engagement system performance modeling results. Here, the LEEDR models are highly pessimistic, mostly resulting in underrated performance relative to measurements. The r_0 of the LEEDR model range from 6 to 10 cm, whereas the HV57 model indicates an r_0 around 34 cm. The profiler r_0 measurements fluctuate significantly, spanning the range of 2–40 cm. These fluctuations in the measurements translate to large fluctuations in the measured open-loop jitter and open-loop Strehl. The open-loop jitter indicated by the LEEDR is 4–5 μrad, whereas the HV57 model shows 1.5 μrad. The profiler measurements fall in between the two models. For context, similar to the ground station, the tracking profiler terminal at the air station also

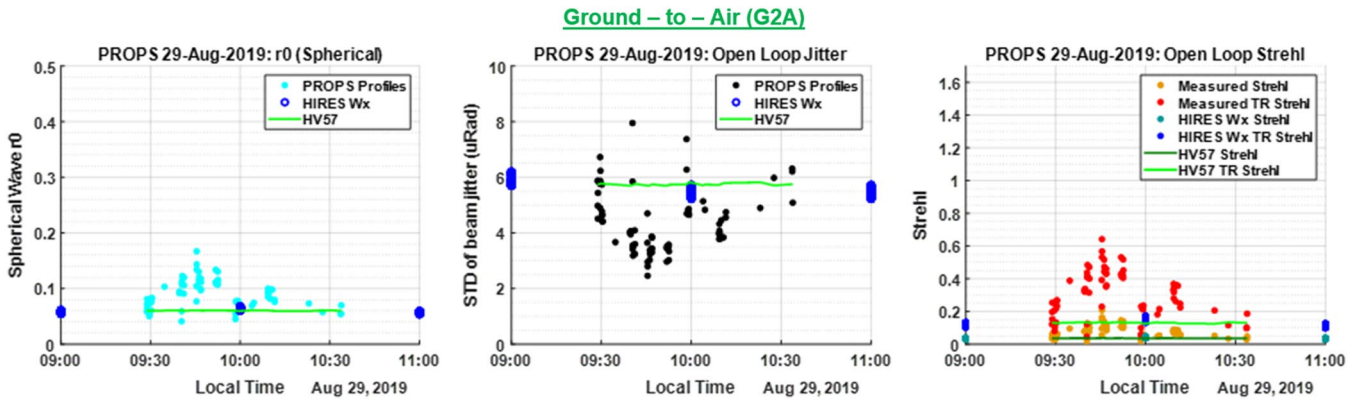

Fig. 13 Ground-to-air system performance.

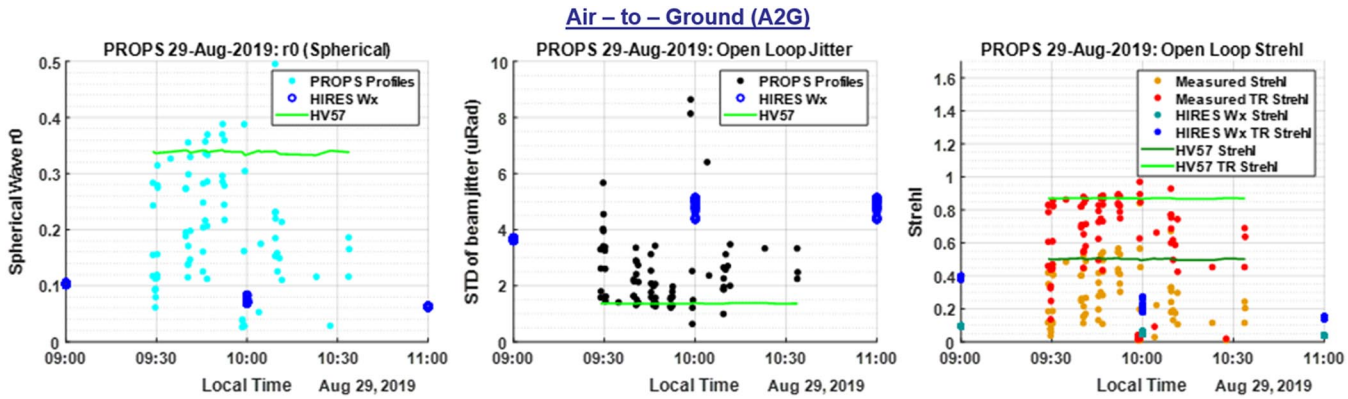

Fig. 14 Air-to-ground system performance.

had two optical systems (acquisition track system and fine track system). The instantaneous field of view of the acquisition track system, which provided the wide field of view, was set to 43.1 μrad, and the instantaneous field of view of the fine track system, which provided the narrow field of view, was set to 7.5 μrad. For an air-to-ground system with similar instantaneous field of views, the jitter created by the uncompensated atmosphere is a negligible fraction of a pixel in the acquisition track system and about 1/5 pixels in the fine track system. The Strehl and tilt-removed Strehl ratios are significantly higher for air to ground engagements as compared with the ground to air system. Because the strong turbulence is away from the aperture, and the aerocontamination has been removed, the air-to-ground system provides more favorable atmospheric conditions for imaging and optical propagation. In Fig. 14, the open-loop Strehl plot (right) shows the HV57 model at 50% and LEEDR spanning 15–40%. The profiler measurements vary from 2 to 60%. The tilt-removed Strehl significantly improves the system performance. The tilt-removed HV57 model and many tilt-removed profiler measurements show a 90% Strehl ratio. Overall, the HV57 model has reasonable agreement with the measurements, whereas the LEEDR model under-rates the air-to-ground system performance.

VII. Conclusions

The work presented here demonstrates a new approach for making air-to-ground path-resolved turbulence measurements. The DDTV path-resolved turbulence profiling technique, along with the described experimental hardware/software tools, enables these types of measurements. Removing the contaminated bins closest to the aircraft allowed atmospheric induced effects to be decoupled from aero-optical contamination. The predicted strength of aero-optical and aero-acoustical contamination showed that the turbulence measurements reasonably isolated the contamination to within the first two bins of the profile. The turbulence profile measurements were compared with the standard HV57 model and state-of-the-art LEEDR atmospheric model. The analysis showed occasional strong agreement in trends between modeling and measurements at higher altitudes. However, the analysis also revealed important deviations between modeling and measurements. The results showed that models consistently predict higher turbulence close to the ground compared with the measurements. However, at altitudes between 1 and 1.5 km, the measurements confirmed a trend seen in the LEEDR model but absent in the HV57 model that shows an increase in C_n^2. The increased turbulence strength at this altitude could be attributed to the Earth boundary layer. The modeling-versus-measurement analysis examined how differences in turbulence profiles impact directed energy system performance parameters. Analyzing system performance metrics such as open-loop jitter and open-loop Strehl shows that conditions are significantly different for air-to-ground and ground-to-air systems operating along the same turbulence path. For the ground-to-air engagements, both models underrated the system performance. For the air-to-ground scenarios, the HV57 model tends to be optimistic and the LEEDR model tends to be pessimistic. The similarities and differences between measurements and models afford an exciting opportunity for future campaigns to build on the findings presented in this paper.

Acknowledgments

We acknowledge and thank the numerous organizations that have supported this research and field measurements. The work presented in this journal paper is a combination of results from two AIAA conference papers (see Refs. [27,28]) and is sponsored by the Joint Transition Office and the Office of Naval Research, grant number ONR N00014-18-1-2112. Special thanks to Mike Zenk and Phil Rollins from University of Notre Dame's Aero-Optics Group for coordinating the experiment and test activities with Northern Jet Management, the aircraft pilots, and the Gerald R. Ford International Airport air traffic control staff. Thank you to the Facilities & Operations coordinators at Coopersville Area Public School (the athletic fields have proven to be an ideal occlusion-free site for the ground station) and to The Air Force Institute of Technology Center for

Directed Energy group for aiding in the development and enhancement of Laser Environmental Effects Definition and Reference (LEEDR) modeling and forecasting. Our advances are built on the outstanding work done with the LEEDR codes. Special thanks to Wright–Patterson Air Force Base (WPAFB) Base Ops, WPAFB Air Field Management staff, WPAFB Security Forces, and Air Force Research Laboratory (AFRL) LADAR Technology branch (AFRL/RYMM) for coordinating and facilitating the numerous long-range preflight ground tests and experiments necessary in support of this flight campaign.

References

[1] Jumper, E. J., Zenk, M. A., Gordeyev, S., Cavalieri, D. A., and Whiteley, M. R., "Airborne Aero-Optics Laboratory," *Optical Engineering*, Vol. 52, No. 7, 2013, Paper 071408.
https://doi.org/10.1117/1.OE.52.7.071408

[2] Gilbert, K. G., and Otten, L. J., *Aero-Optical Phenomena*, Vol. 80, Progress in Astronautics and Aeronautics, AIAA, Reston, VA, 1982.

[3] Sutton, G., "Aero-Optical Foundations and Applications," *AIAA Journal*, Vol. 23, No. 10, 1985, pp. 1525–1537.
https://doi.org/10.2514/3.9120

[4] Porter, C., Gordeyev, S., and Jumper, E. J., "Flight Measurements of the Aero-Optical Environment Around a Flat-Windowed Turret," *AIAA Journal*, Vol. 51, No. 6, 2013, pp. 1394–1403.
https://doi.org/10.2514/1.J052067

[5] Delucca, N., Gordeyev, S., and Jumper, E. J., "In-Flight Aero-Optics of Turrets," *Optical Engineering*, Vol. 52, No. 7, 2013, Paper 071405.
https://doi.org/10.1117/1.OE.52.7.071405

[6] Andrews, L. C., and Phillips, R. L., *Laser Beam Propagation Through Random Media*, SPIE, Bellingham, Washington, D.C., 2005.
https://doi.org/10.1117/3.626196

[7] Tyson, R. K., *Introduction to Adaptive Optics*, Vol. 41, SPIE, Bellingham, Washington, D.C., 2000.
https://doi.org/10.1117/3.358220

[8] Tatarskii, V., *Wave Propagation in a Turbulent Medium*, McGraw–Hill, New York, Jan. 1961, pp. 1–285.

[9] Whiteley, M. R., "Rytov Parameter Estimation by Use of Differential-Tilt Measurements," *Propagation and Imaging Through the Atmosphere IV*, Vol. 4125, edited by Roggemann, M. C., SPIE, Nov. 2000, pp. 7–20.
https://doi.org/10.1117/12.409299

[10] Klückers, V., Wooder, N., Nicholls, T., Adcock, M., Munro, I., and Dainty, J., "Profiling of Atmospheric Turbulence Strength and Velocity Using a Generalised SCIDAR Technique," *Astronomy and Astrophysics Supplement Series*, Vol. 130, No. 1, 1998, pp. 141–155.
https://doi.org/10.1051/aas:1998217

[11] Lambert, A., Jenkins, C., and Goodwin, M., "Turbulence Profiling Using Extended Objects for Slope Detection and Ranging (SLODAR)," *Image Reconstruction from Incomplete Data IV*, Vol. 6316, edited by P. J. Bones, M. A. Fiddy, and R. P. Millane, SPIE, Bellingham, Washington, D.C., Sept. 2006, pp. 1–11.
https://doi.org/10.1117/12.682428

[12] Goodwin, M., Jenkins, C., and Lambert, A., "Improved Detection of Atmospheric Turbulence with SLODAR," *Optics Express*, Vol. 15, No. 22, 2007, pp. 14,844–14,860.
https://doi.org/10.1364/OE.15.014844

[13] de la Nuez Cruz, A., García-Lorenzo, B., Fuensalida, J. J., and Rodríguez-Hernández, M. A. C., "Atmospheric Turbulence Profiling at the Teide Observatory: Comparison and Calibration of SODAR and SCIDAR Measurements," *Optics in Atmospheric Propagation and Adaptive Systems X*, Vol. 6747, edited by K. Stein, A. Kohnle, and J. D. Gonglewski, SPIE, Oct. 2007, pp. 240–248.
https://doi.org/10.1117/12.737749

[14] Brennan, T. J., and Mann, D. C., "Estimation of Optical Turbulence Characteristics from Shack Hartmann Wavefront Sensor Measurements," *Advanced Wavefront Control: Methods, Devices, and Applications VIII*, Vol. 7816, edited by D. C. Dayton, T. A. Rhoadarmer, and D. J. Sanchez, SPIE, Bellingham, Washington, D.C., Aug. 2010, pp. 9–24.
https://doi.org/10.1117/12.862808

[15] Cortés, A., Neichel, B., Guesalaga, A., Osborn, J., Rigaut, F., and Guzman, D., "Atmospheric Turbulence Profiling Using Multiple Laser Star Wavefront Sensors," *Monthly Notices of the Royal Astronomical Society*, Vol. 427, No. 3, 2012, pp. 2089–2099.
https://doi.org/10.1111/j.1365-2966.2012.22076.x

[16] Laidlaw, D. J., Osborn, J., Wilson, R. W., Morris, T. J., Butterley, T., Reeves, A. P., Townson, M. J., Gendron, É., Vidal, F., and Morel, C., "Turbulence Profiling for Adaptive Optics Tomographic Reconstructors," *Adaptive Optics Systems V*, Vol. 9909, edited by E. Marchetti, L. M. Close, and L.-P. Véran, SPIE, July 2016, pp. 1102–1107.
https://doi.org/10.1117/12.2233323

[17] Schmidt, J., and Whiteley, M. R., "Range-Resolved Turbulence Profiling with a Wavefront Sensor and Cooperative Source," *OSA: Propagation Through and Characterization of Atmospheric and Oceanic Phenomena*, Optical Soc. of America, Washington, D.C., 2019, pp. 1–26.

[18] McCrae, J. E., Bose-Pillai, S., Current, M., Lee, K., and Fiorino, S., "Analysis of Turbulence Anisotropy with a Hartmann Sensor," *Propagation Through and Characterization of Atmospheric and Oceanic Phenomena*, Optical Soc. of America, Washington, D.C., 2017, Paper PTu2D.3.
https://doi.org/10.1364/PCAOP.2017.PTu2D.3

[19] McCrae, J. E., Bose-Pillai, S. R., Current, M. G., Lee, K. P., and Fiorino, S. T., "Measurements of Anisotropy in Optical Turbulence," *2017 IEEE Aerospace Conference*, Inst. of Electrical and Electronics Engineers, New York, 2017, pp. 1–7.
https://doi.org/10.1109/AERO.2017.7943660

[20] McCrae, J. E., Bose-Pillai, S. R., Fiorino, S. T., Archibald, A. J., Meoak, J., Elmore, B. J., Kesler, T., and Rice, C. A., "Measurements of Optical Turbulence over 149-km Path," *Optical Engineering*, Vol. 59, No. 8, 2020, Paper 081806.
https://doi.org/10.1117/1.OE.59.8.081806

[21] Zuraski, S. M., Beecher, E., McCrae, J. E., and Fiorino, S. T., "Turbulence Profiling Using Pupil Plane Wavefront Data Derived Fried Parameter Values for a Dynamically Ranged Rayleigh Beacon," *Optical Engineering*, Vol. 59, No. 8, 2020, Paper 081807.
https://doi.org/10.1117/1.OE.59.8.081807

[22] Andrews, L. C., Phillips, R. L., and Hopen, C. Y., *Laser Beam Scintillation with Applications*, Vol. 99, SPIE, Bellingham, Washington, D.C., 2001, Chaps. 1–10.
https://doi.org/10.1117/3.412858

[23] Whiteley, M. R., Washburn, D. C., and Wright, L. A., "Differential-Tilt Technique for Saturation-Resistant Profiling of Atmospheric Turbulence," *Adaptive Optics Systems and Technology II*, Vol. 4494, edited by R. K. Tyson, D. Bonaccini, and M. C. Roggemann, SPIE, Bellingham, Washington, D.C., Feb. 2002, pp. 221–232.
https://doi.org/10.1117/12.454795

[24] Sasiela, R. J., *Electromagnetic Wave Propagation in Turbulence: Evaluation and Application of Mellin Transforms*, Vol. 18, SPIE, Bellingham, Washington, D.C., 2012, Chaps. 1–12.
https://doi.org/10.1117/3.741372

[25] Noll, R. J., "Zernike Polynomials and Atmospheric Turbulence," *Journal of the Optical Society of America*, Vol. 66, No. 3, 1976, pp. 207–211.
https://doi.org/10.1364/JOSA.66.000207

[26] Whiteley, M. R., Welsh, B. M., and Roggemann, M. C., "Optimal Modal Wave-Front Compensation for Anisoplanatism in Adaptive Optics," *Journal of the Optical Society of America A*, Vol. 15, No. 8, 1998, pp. 2097–2106.
https://doi.org/10.1364/JOSAA.15.002097

[27] Kalensky, M., Jumper, E. J., Whiteley, M. R., Diskin, Y., Gordeyev, S., Drye, R., Archibald, A., and Grose, M., "Turbulence Profiling Using AAOL-BC," *AIAA Scitech 2020 Forum*, AIAA Paper 2020-0682, 2020.
https://doi.org/10.2514/6.2020-0682

[28] Diskin, Y., Grose, M., Whiteley, M., Kalensky, M., Jumper, E., Gordeyev, S., and Archibald, A., "Atmospheric and Aero Disturbance Characterization for DE System Applications," *AIAA AVIATION 2020 FORUM*, AIAA Paper 2020-3234, 2020.
https://doi.org/10.2514/6.2020-3234

[29] Kalensky, M., Gordeyev, S., and Jumper, E. J., "In-Flight Studies of Aero-Optical Distortions Around AAOL-BC," *AIAA Aviation 2019 Forum*, AIAA Paper 2019-3253, 2019.
https://doi.org/10.2514/6.2019-3253

[30] Kalensky, M., Wells, J., Jumper, E. J., and Gordeyev, S., "Image Degradation Due to Various Aero-Optical Environments," *Proceedings of SPIE*, Vol. 11102, edited by E. Novak, and J. D. Trolinger, SPIE, Bellingham, Washington, D.C., Sept. 2019, pp. 109–120.
https://doi.org/10.1117/12.2528509

[31] Gordeyev, S., and Kalensky, M., "Effects of Engine Acoustic Waves on Aerooptical Environment in Subsonic Flight," *AIAA Journal*, Vol. 58, No. 12, 2020, pp. 5306–5317.
https://doi.org/10.2514/1.J059484

[32] Kalensky, M., Wells, J., and Gordeyev, S. A., "Image Degradation Due to Different in-Flight Aero-Optical Environments," *Optical Engineering*, Vol. 59, No. 10, 2020, Paper 104104.
https://doi.org/10.1117/1.OE.59.10.104104

[33] Gordeyev, S., Smith, A. E., Cress, J. A., and Jumper, E. J., "Experimental Studies of Aero-Optical Properties of Subsonic Turbulent Boundary Layers," *Journal of Fluid Mechanics*, Vol. 740, Feb. 2014, p. 214. https://doi.org/10.1017/jfm.2013.658

[34] Andrews, L. C., Phillips, R. L., Wayne, D., Leclerc, T., Sauer, P., Crabbs, R., and Kiriazes, J., "Near-Ground Vertical Profile of Refractive-Index Fluctuations," *Proceedings of SPIE*, Vol. 7324, edited by L. M. W. Thomas, and G. C. Gilbreath, SPIE, Bellingham, Washington, D.C., April 2009, pp. 11–12. https://doi.org/10.1117/12.820369

[35] Fiorino, S. T., Bartell, R. J., Krizo, M. J., Caylor, G. L., Moore, K. P., Harris, T. R., and Cusumano, S. J., "A First Principles Atmospheric Propagation & Characterization Tool: The Laser Environmental Effects Definition and Reference (LEEDR)," *Atmospheric Propagation of Electromagnetic Waves II*, Vol. 6878, edited by O. Korotkova, SPIE, Bellingham, Washington, D.C., Feb. 2008, pp. 57–68. https://doi.org/10.1117/12.763812

[36] Gravley, L. E., "Comparison of Climatological Optical Turbulence Profiles to Standard, Statistical and Numerical Models Using HELEEOS," Air Force Inst. of Technology AFIT-GAP-ENP-06-06, Wright–Patterson AFB, OH, 2006.

[37] Thomas, G., Cobb, R., Fiorino, S., and Hawks, M., "Daytime Cloudless Sky Radiance Quantification with Ground-Based Aerosol and Meteorological Observations in the Shortwave Infrared," *Journal of Atmospheric and Oceanic Technology*, Vol. 37, No. 5, 2020, pp. 777–788. https://doi.org/10.1175/JTECH-D-19-0157.1

[38] Stull, R. B., *An Introduction to Boundary Layer Meteorology*, Vol. 13, Springer, New York, 1988, pp. 1–27, Chap. 1.

[39] Oke, T. R., *Boundary Layer Climates*, Routledge, Abingdon, U.K., Jan. 1988, pp. 1–464.

[40] Jumper, E. J., and Fitzgerald, E. J., "Recent Advances in Aero-Optics," *Progress in Aerospace Sciences*, Vol. 37, No. 3, 2001, pp. 299–339. https://doi.org/10.1016/S0376-0421(01)00008-2

[41] De Lucca, N., Gordeyev, S., and Jumper, E. J., "The Airborne Aero-Optics Laboratory, Recent Data," *Acquisition, Tracking, Pointing, and Laser Systems Technologies XXVI*, Vol. 8395, edited by W. E. Thompson, and P. F. McManamon, SPIE, Bellingham, Washington, D.C., May 2012, pp. 60–70. https://doi.org/10.1117/12.923074

[42] Jumper, E. J., Gordeyev, S., Cavalieri, D., Rollins, P., Whiteley, M. R., and Krizo, M., "Airborne Aero-Optics Laboratory-Transonic (AAOL-T)," *53rd AIAA Aerospace Sciences Meeting*, AIAA Paper 2015-0675, 2015. https://doi.org/10.2514/6.2015-0675

[43] Shellan, J. B., "Statistical Properties of the Strehl Ratio as a Function of Pupil Diameter and Level of Adaptive Optics Correction Following Atmospheric Propagation," *Journal of the Optical Society of America A*, Vol. 21, No. 8, 2004, pp. 1445–1451. https://doi.org/10.1364/JOSAA.21.001445

[44] Widiker, J. J., and Magee, E. P., "Open-Loop Simulations of Atmospheric Turbulence Using the AdAPS Interface," *Advanced Wavefront Control: Methods, Devices, and Applications III*, Vol. 5894, edited by M. T. Gruneisen, J. D. Gonglewski, and M. K. Giles, SPIE, Bellingham, Washington, D.C., Aug. 2005, pp. 35–44. https://doi.org/10.1117/12.617031

[45] Valley, G. C., "Long-and Short-Term Strehl Ratios for Turbulence with Finite Inner and Outer Scales," *Applied Optics*, Vol. 18, No. 7, 1979, pp. 984–987. https://doi.org/10.1364/AO.18.000984

L. Ukeiley
Associate Editor